Chapter 5

Buncher and Ionization Cooling

In this Chapter, the Buncher and SFOFO cooling channel are introduced and described. Performance, systematic errors and tolerances are discussed. Design of the LH_2 absorbers is included here, in Section 5.3.6. Design of the rf components and superconducting solenoid magnets are discussed in Chapters 8 and 10, respectively.

The designs presented here for the bunching and cooling channels employ a variety of magnetic-focusing lattices. In these lattices, the solenoidal magnetic field is periodically reversed in order to modulate the beta function, producing periodic minima and maxima of beta, typically with local secondary minima and maxima located in between (see Fig. 5.6). To be specific in our descriptions, we here define a "cell" to be that portion of apparatus extending from one beta minimum to the next (for example, from one liquid-hydrogen absorber to the next in the SFOFO cooling lattice described below). Note that one cell of such a lattice thus corresponds to a half-period of the magnetic field.

5.1 Matching Section from the Induction Linac to the Buncher.

After the energy spread of the beam has been reduced in the induction linacs, the muons are distributed continuously over a distance of about 100 m. It is then necessary to form the muons into a train of bunches prior to cooling and subsequent acceleration. First, an 11-m-long magnetic lattice section (four 2.75 m cells) is used to gently transform the beam from the approximately uniform solenoidal field used in the induction linacs to the so-called "super-FOFO," or SFOFO, lattice used in the remainder of the front end. This is followed by the 55-m-long rf buncher itself, which consists of rf cavity sections interspersed with drift regions. These two functions are performed sequentially for design simplicity.

There is a significant advantage in using the same lattice in the buncher section as in the cooling region to follow, since it avoids adding another complicated 6-dimensional matching section.

Two distinct computer codes were used to simulate this buncher and the cooling channel: ICOOL [1] and Geant4 [2]. There is no shared code between the two programming environments: Fortran for ICOOL and C++ for Geant4. The Geant4 and ICOOL implementations were based solely on the parameters listed below. After optimization, good agreement between these two codes was obtained, as shown in the performance section. Thus, we have high confidence that the simulated cooling performance is realistic.

5.1.1 The Transverse Matching Section

The purpose of the transverse matching section is to transform the muon beam smoothly from the approximately uniform 1.25 T focusing field in the induction linac to the 2 T alternating polarity SFOFO lattice. The 4% rms momentum spread entering the matching section is relatively small, so chromatic corrections are less critical than in the minicooling field reversal. Table 5.1 gives coil dimensions and current densities for the solenoid magnets used in the matching simulations.

Table 5.1: Matching section magnets.

z (m)	dz (m)	r (m)	dr (m)	j (A/mm^2)
0.358	1.375	0.300	0.100	-9.99
1.733	0.330	0.300	0.110	-15.57
2.446	0.187	0.330	0.330	-33.40
2.963	0.187	0.330	0.330	35.19
4.008	0.330	0.770	0.110	67.41
5.146	0.187	0.330	0.330	43.75
5.663	0.187	0.330	0.330	-43.75
6.708	0.330	0.770	0.110	-66.12
7.896	0.187	0.330	0.330	-43.75
8.413	0.187	0.330	0.330	43.75
9.458	0.330	0.770	0.110	66.12
10.646	0.187	0.330	0.330	43.75

The magnet configuration at the beginning of the section, the axial magnetic field on-axis, and the beta functions for three momenta are shown in Fig. 5.1. The magnetic lattice

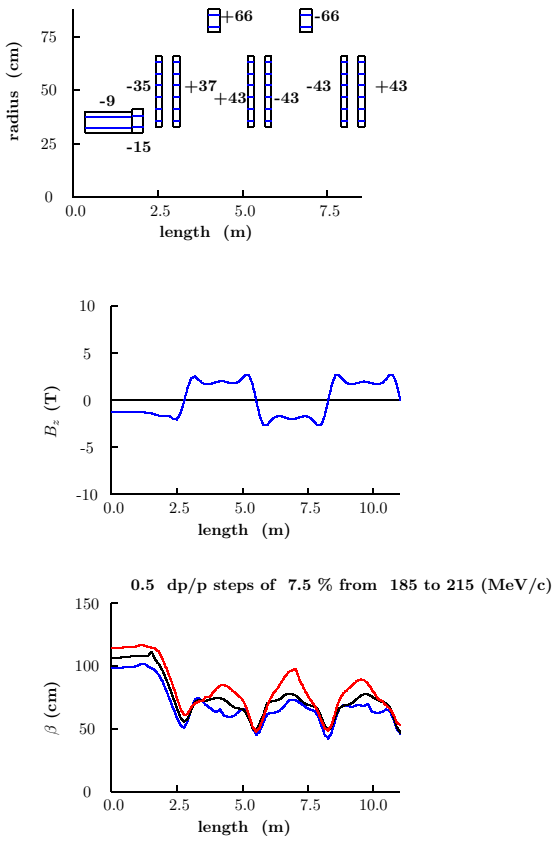

Figure 5.1: Magnet configuration, axial magnetic field and beta function of the matching section to the SFOFO lattice.

goes from a series of constant radius solenoids to an SFOFO cell structure consisting of small radius coils at each end of a cell and a large radius coil in the middle. The axial magnetic field in a cell peaks symmetrically near the two ends and has a smaller secondary peak in the middle. The beta functions across the match are similar for the three momenta shown, which vary in momentum steps of 7.5% from 185 to 215 MeV/c.

5.2 Buncher Section

The design principles for the lattice and details concerning the rf and other technical components for the buncher section will be described later. Only the beam dynamics and performance will be described here.

The buncher magnetic lattice is identical to that used in the first cooling section. It contains rf cavities in selected lattice cells and no absorbers. The main rf frequency was chosen to be 201.25 MHz in the front end, so that the beam would fit radially inside the cavity aperture. Power sources and other technical components are available at this frequency. The 201.25 MHz cavities are placed at the high-beta locations in the lattice, just as in the cooling section. Harmonic cavities running at 402.5 MHz are placed at minimum-beta locations, corresponding to where hydrogen absorbers are placed in the cooling section.

The buncher comprises 20 lattice cells, each 2.75 m long. Maximum bunching efficiency is obtained by breaking the region into three rf stages, separated by drift regions. The locations and lengths of the buncher components are given in Table 5.2.

Second harmonic (402.5 MHz) cavities are used at the entrance and exit of the first and second stages to linearize the shape of the rf pulse. All cavities are assumed to have thin Be windows at each end. They are modeled in the simulation codes as perfect TM_{010} pillboxes. The window radii and thicknesses are given in Table 8.5. The electric field gradient in the buncher ranges from 6 to 8 MV/m. A long drift is provided after the first stage to allow the particles to begin overlapping in space.

Figs. 5.2 and 5.3 show the momentum-time distributions at the start, and after each of the three buncher stages. Distributions are also shown at the ends of the first and second cooling stages. In the last three distributions, ellipses are drawn indicating the approximate acceptance of the cooling channel.

It can be seen that, at the end of the buncher, most, but not all, particles are within the approximately elliptical bucket. About 25% are outside the bucket and are lost relatively rapidly, and another 25% are lost in the cooling channel as the longitudinal emittance rises due to straggling and the negative slope of the dE/dx curve with energy.

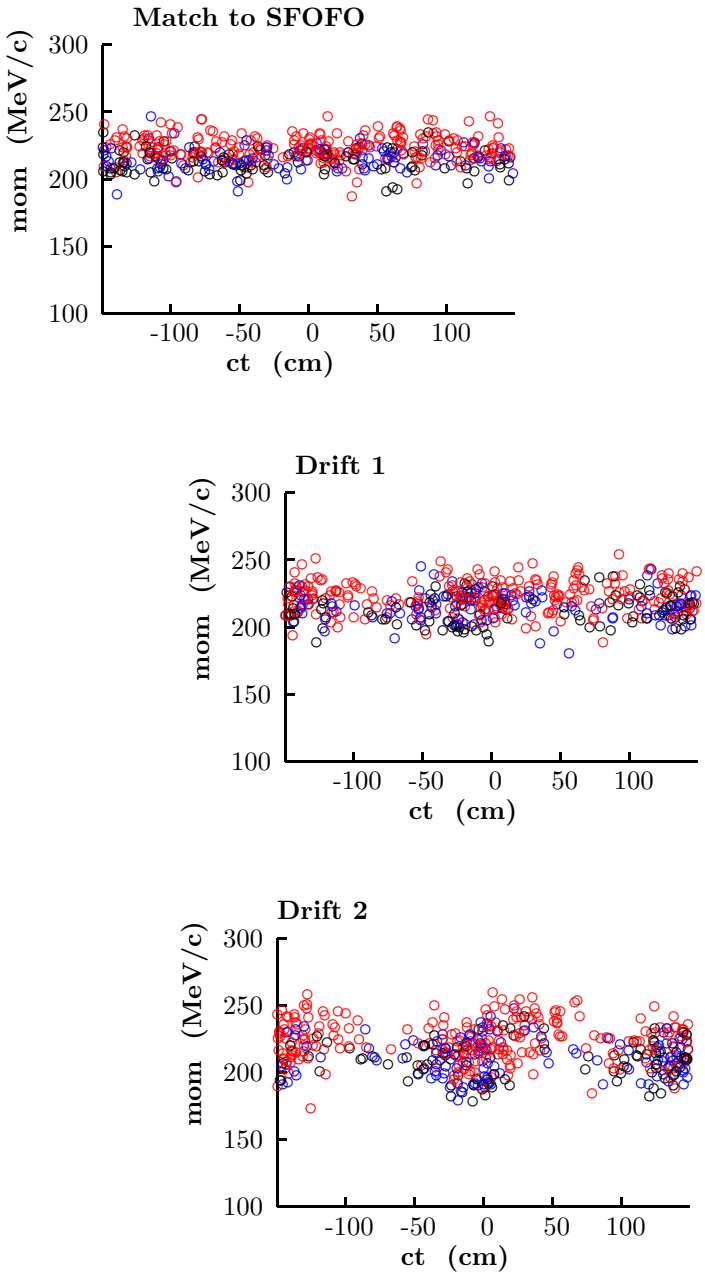

Figure 5.2: Momentum-time distributions through the buncher.

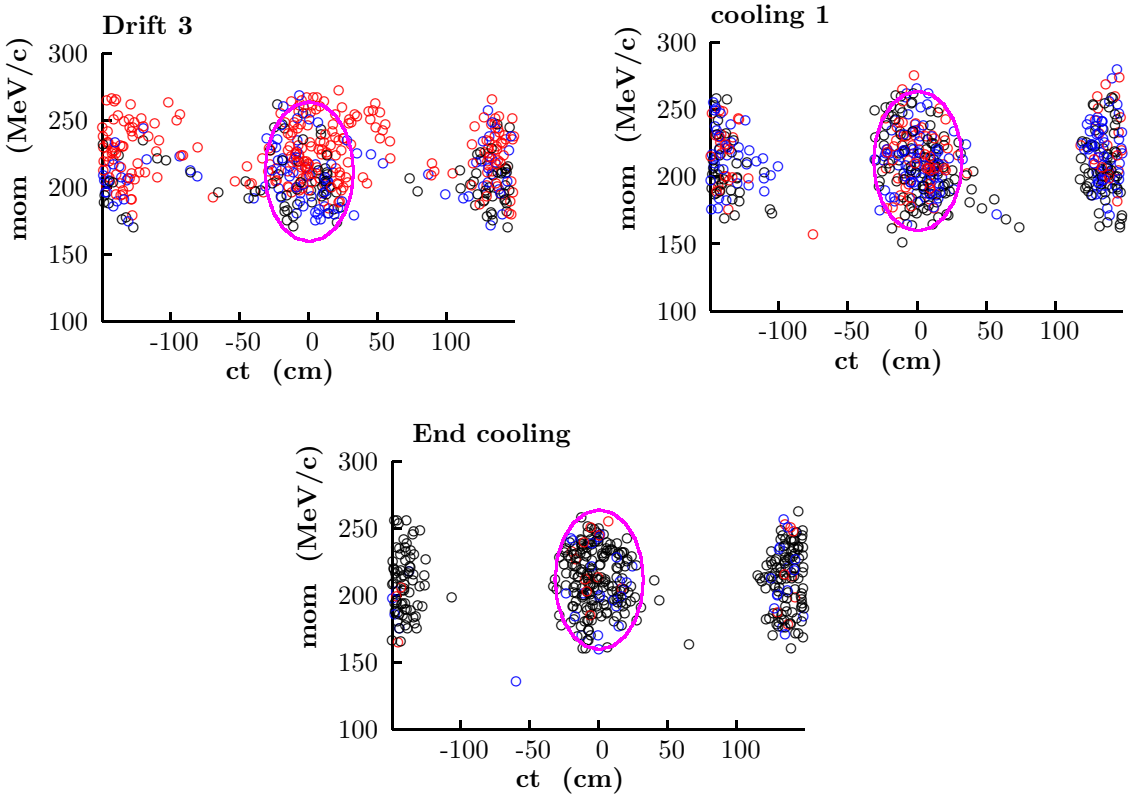

Figure 5.3: Momentum-time distributions through the buncher (continued).

5.2.1 Longitudinal-Transverse Correlation

A significant coupling develops in these pre-cooling stages of the Neutrino Factory (including the induction linac) between a particle's longitudinal and transverse motions. This occurs because particles with different transverse displacements, or angular divergences, take different amounts of time to move axially down the solenoidal lattice. They thus arrive at the cavities at different points in the rf cycle, or at a different time with respect to the induction linac pulse, thereby obtaining different accelerations and velocities. The resulting correlation, shown in Fig. 5.4, can be expressed as

$$p = p_o + CA^2, \tag{5.1}$$

where C is the correlation coefficient and the transverse amplitude is defined as

$$A^2 = \frac{r^2}{\beta_\perp^2} + \theta^2. \tag{5.2}$$

This quantity is evaluated at a waist in the transverse plane.

The magnitude of the momentum-amplitude correlation coefficient is seen from Fig. 5.4 to be 0.7 GeV/c. This is a higher value than the 0.45 GeV/c that would be obtained without the minicooling. Ideally, the correlation should be such that forward velocity in the following lattice is independent of transverse amplitude. A value of approximately 1.1 GeV/c would be required for this.

Figure 5.4 shows also that there is little correlation between momentum and angular momentum after the induction linacs, indicating that the field reversal in the minicooling is correctly located with respect to the induction linacs.

5.3 Ionization Cooling Channel

The rms transverse emittance of the muon beam emerging from the induction linac must be reduced to ≈ 2 mm·rad (normalized) in order to fit into the downstream accelerators and be contained in the storage ring. Ionization cooling is currently our only feasible option [3]. The cooling channel described below, as well as the one described in the appendix, are based on extensive theoretical studies and computer simulations performed in the same context as our previous studies [4, 3, 5, 6].

5.3.1 Principle of Ionization Cooling

In ionization cooling, the beam loses both transverse and longitudinal momentum by ionization energy loss while passing through an absorber. The longitudinal momentum

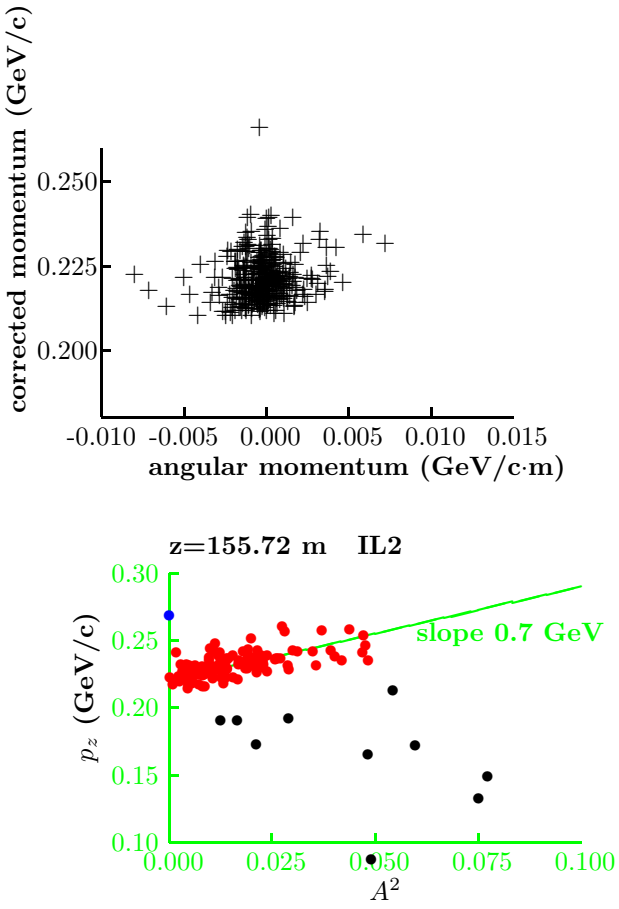

Figure 5.4: (top) Correlation between momentum and angular momentum; (bottom) correlation between longitudinal momentum and transverse amplitude (see Eq. 5.2), after the induction linac (IL2).

is then restored to the beam in rf accelerating cavities. This sequence, repeated many times, results in a reduction of the angular spread and thereby reduces the transverse emittance.

Ionization cooling is limited by multiple Coulomb scattering (MCS) in the absorbers. To minimize the MCS effect on cooling channel performance, we must have rather strong focusing at the absorber, with $\beta_{\perp,min} \approx 0.4$ to 0.2 m at a momentum of 200 MeV/c. Strong solenoidal fields are used for this purpose. Weak focusing, *i.e.*, too large $\beta_\perp$ at the absorbers, leads to excessive emittance growth due to MCS. Too strong focusing is hard to achieve for such large aperture beam transport, but can also be detrimental to the 6D beam dynamics. As the angles, or beam divergence, get too large, the longitudinal velocity decreases too much, leading to the wrong longitudinal-transverse correlation factor and thereby resulting in unacceptable growth of the longitudinal emittance. Choosing the right range of $\beta_{\perp,min}$ with respect to the operating momentum is a key to a successful design [3, 6].

The approximate equation for transverse cooling in a step ds along the particle's orbit is [4]

$$\frac{d\epsilon_N}{ds} = -\frac{1}{\beta^2}\frac{dE_\mu}{ds}\frac{\epsilon_N}{E_\mu} + \frac{\beta_\perp (0.014\text{GeV})^2}{2\beta^3 E_\mu m_\mu L_R}, \tag{5.3}$$

where β is the normalized velocity, E_μ is the total energy, m_μ is the muon mass, ϵ_N is the normalized transverse emittance, $\beta_\perp$ is the betatron function at the absorber, dE_μ/ds is the energy loss per unit length, and L_R is the radiation length of the absorber material. The betatron function is determined by the strengths of the elements in the focusing lattice. Together with the beam emittance, the beta function determines the local size and divergence of the beam. (Note that the energy loss dE_μ/ds is defined here as a positive quantity, unlike the convention often used in particle physics.) The first term in this equation is the cooling term, and the second describes the heating due to multiple scattering. The heating term is minimized if $\beta_\perp$ is small (strong focusing) and L_R is large (a low-Z absorber).

The minimum normalized transverse emittance that can be achieved for a given absorber in a given focusing field is reached when the cooling rate equals the heating rate in Eq. 5.3,

$$\epsilon_{N,min} = \frac{\beta_\perp (14\text{MeV})^2}{2\beta m_\mu \frac{dE_\mu}{ds} L_R}. \tag{5.4}$$

For a relativistic ($\beta \approx 0.87$) muon in liquid hydrogen with a beta function $\beta_\perp = 8$ cm, which corresponds roughly to confinement in a 15 T solenoidal field, the minimum achievable emittance is about 340 mm·mrad.

The equation for energy spread is

$$\frac{d(\Delta E_\mu)^2}{ds} = -2\,\frac{d\left(\frac{dE_\mu}{ds}\right)}{dE_\mu}\langle(\Delta E_\mu)^2\rangle + \frac{d(\Delta E_\mu)^2_{\rm stragg}}{ds} \tag{5.5}$$

where the first term describes the cooling or heating due to energy loss, and the second term describes the heating due to straggling. ΔE_μ is the rms spread in the energy of the beam.

Ionization cooling of muons seems relatively straightforward in theory, but requires simulation studies and hardware development for its optimization and application. There are practical problems in designing lattices that can transport and focus the large emittance beam. There will also be effects from space charge and wake fields, if the beam intensity is sufficiently high.

We have developed a number of tools for studying the ionization cooling process. First, the basic theory was used to identify the most promising beam properties, material type and focusing arrangements for cooling. Given practical limits on magnetic field strengths, this gives an estimate of the minimum achievable emittance for a given configuration. Next several tracking codes were written, or modified, to study the cooling process in detail. These codes use Monte Carlo techniques to track particles one at a time through the cooling system. The codes attempt to include all relevant physical processes (*e.g.*, energy loss, straggling, multiple scattering), and use physically correct electromagnetic fields.

5.3.2 Concept of the Tapered SFOFO Cooling Channel

For optimal performance, the solenoidal field should not be kept constant during the entire cooling process. In a cooling channel with a constant solenoidal field, the transverse momentum of each particle will decrease, while the position of the Larmor center will not, causing the net angular momentum of the beam to grow. To avoid this, we flip the field while maintaining good focusing throughout the beam transport and low $\beta_\perp$ at the absorbers. One of the simplest solutions (the FOFO lattice), is to vary the field sinusoidally. The transverse motion in such a lattice can be characterized by its betatron resonances, near which the motion is unstable. The stable operating region is between the low momentum (2π) and high momentum (π) phase advance per half-period of the lattice. (Note that a half-period of the lattice is one "cell" in our notation.) The SFOFO lattice [7] is based on the use of alternating solenoids, but is a bit more complicated. We add a second harmonic to the simple sinusoidal field, producing the axial field shown in Fig. 5.5. As in the FOFO case, the axial field vanishes at the $\beta_{\perp,min}$ position, located at

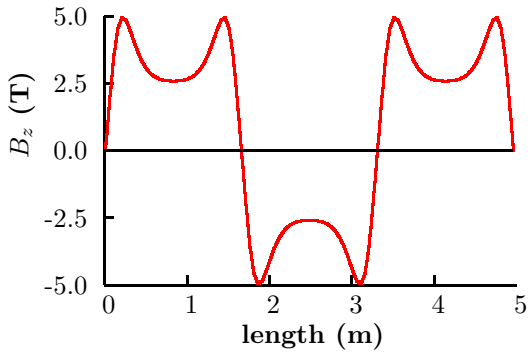

Figure 5.5: The longitudinal component of the on axis magnetic field, B_z, for a typical SFOFO lattice.

the center of the absorber. This is accomplished by using two short *focusing* coils running in opposite polarity. However, unlike the FOFO case, the field decreases and flattens at $\beta_{\perp,max}$, due to a *coupling* coil located midway between the focusing coils, around the rf cavity. The transverse beam dynamics is strongly influenced by the solenoidal field profile on-axis and by the desired range of momentum acceptance.

This SFOFO lattice has several advantages over the FOFO:

- The betatron resonances are usually a nuisance, since they inevitably restrict the region of stable motion. However, in this case they give us a strong, approximately constant, focusing result (*i.e.*, flat $\beta_\perp$) across the relevant momentum range, as we operate between the 2π and π resonances. This is illustrated in Figs. 5.6 and 5.7. Within this (albeit limited) momentum range the transverse motion is stable.

- For a given $\beta_{\perp,min}$, the SFOFO period is longer than the corresponding FOFO period, allowing longer absorbers per lattice cell, thereby reducing the relative amount of multiple scattering in the absorber windows. The longer period also allows more room for all other components.

- The focusing coils can be located just around the absorbers, adjacent to the rf cavity. Since the absorber has a much smaller outer diameter than does the rf cavity, this arrangement allows the diameter of these high-field magnets to be reduced considerably, with concomitant cost savings.

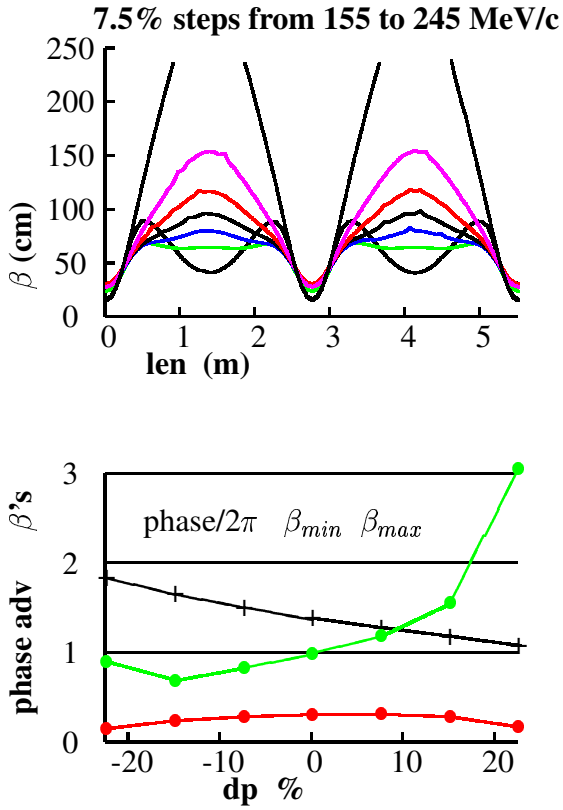

Figure 5.6: (top) Beta functions in the (1,3) cooling lattice section, at small transverse amplitude, for 7 different momenta, spanning the entire operating range from 155 to 245 MeV/c above the 2π and below the π resonance. (bottom) $\beta_{\rm min}, \beta_{\rm max}$ and phase advance as a function of relative momentum. The lower curve corresponds to $\beta_{\rm min}$ and the second curve from the bottom to the phase advance. The black crosses show the $\beta_{\rm max}$ function.

Table 5.2: RF buncher component locations used in the simulations.

	Length (m)	Frequency (MHz)	Phase (deg.)	Gradient (MV/m)
Harmonic rf	0.186	402.5	180	6.4
Space	0.443			
rf	4×0.373	201.25	0	6.4
Space	0.443			
Harmonic rf	0.186	402.5	180	6.4
Drift 1	10×2.75			
Harmonic rf	0.186	402.5	180	6
Space	0.443			
rf	4×0.373	201.25	0	6
Space	0.443			
Harmonic rf	2×0.186	402.5	180	6
Space	0.443			
rf	4×0.373	201.25	0	6
Space	0.443			
Harmonic rf	0.186	402.5	180	6
Drift 2	3×2.75			
Space	0.629			
rf	4×0.373	201.25	12	8
Space	0.629			
Space	0.629			
rf	4×0.373	201.25	12	8
Space	0.629			
Drift 3	2×2.75			

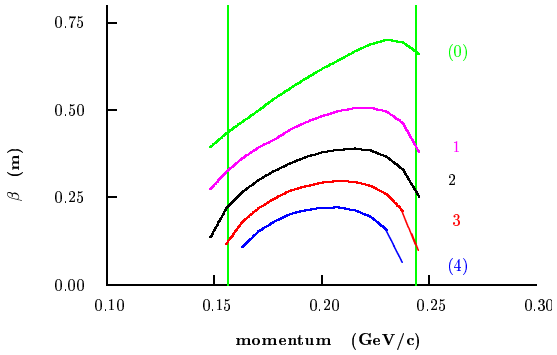

Figure 5.7: The $\beta_\perp$ function versus momentum for the five SFOFO lattices described below.

For a given lattice period, one can adjust independently the location of the two betatron resonances, or, equivalently, the nominal operating momentum and the $\beta_{\perp,min}$ at that momentum. By adjusting these two parameters, we can keep the $\beta_\perp$ symmetric about the required nominal momentum, and independently reduce the central $\beta_\perp$ value. However, this is true over only a limited momentum range. As we decrease the coupling field and increase the focusing field, the momentum acceptance will shrink as the π and 2π resonances move closer to the nominal momentum. At this point, we are forced to change the lattice period.

This brings us to the second improvement over the FOFO channel used in the previous feasibility study: $\beta_{\perp,min}$ can be "tapered" along the cooling channel. One can slowly increase the focusing strength at a fixed operating momentum, while keeping a reasonable momentum acceptance. Were we to use a fixed $\beta_{\perp,min}$, as the cooling progresses, the rms angle would decrease. The cooling rate would then also decrease as the heating term due to multiple scattering becomes relatively more important. By slowly increasing the focusing strength (decreasing $\beta_{\perp,min}$), we can maintain large rms angles at the absorbers ($\sigma_{x'} = \sigma_{y'} \approx 0.1$ rad), thereby keeping the relative effect of multiple scattering to a minimum.

5.3.3 Description of the SFOFO Cooling Channel

In this subsection, we describe the cooling channel from the viewpoint of the simulation effort. Engineering details will be given later.

5.3.3.1 Lattices

The channel operates at a nominal momentum of 200 MeV/c. There are six sections with steadily decreasing $\beta_{\perp,min}$. In the first three lattices, labeled (1,i), i=1,3, the lattice cell length is 2.75 m, and in the other three lattices, (2,i), i=1,3, it is 1.65 m. A cell of the cooling lattice comprises one absorber, one linac and three coils. The matching sections between these sections also consist of cooling cells, which differ from the regular cooling cells only by the current circulating in the coils, with one exception: A different coil length must be used in the matching section between the (1,3) and (2,1) lattices, where the cell length decreases from 2.75 m to 1.65 m. The lengths of these lattice sections are specified in Table 5.3. Coil dimensions and current densities are specified in Table 5.4. In the simulations, it is assumed that the current density is uniform across the thickness of the coil.

Table 5.3: Lengths of the sections and integrated length from the start of the cooling channel.

Section	Length (m)	Total length (m)
Cool (1,1)	$4 \times 2.75 = 11$	11
Match (1,1-2)	$2 \times 2.75 = 5.5$	16.5
Cool (1,2)	$4 \times 2.75 = 11$	27.5
Match (1,2-3)	$2 \times 2.75 = 5.5$	33
Cool (1,3)	$4 \times 2.75 = 11$	44
Match (1,3) - (2,1)	4.4	48.4
Cool (2,1)	$12 \times 1.65 = 19.8$	68.2
Match (2,1-2)	$2 \times 1.65 = 3.3$	71.5
Cool (2,2)	$8 \times 1.65 = 13.2$	84.7
Match (2,2-3)	$2 \times 1.65 = 3.3$	88
Cool (2,3)	$12 \times 1.65 = 19.8$	107.8

The design of the matching sections between regular sections of the same cell length goes as follows. In all cases, a matching section is inserted that consists of two lattice

Table 5.4: Geometry and current densities for the solenoids used in the simulations. The j(1,n) coil types refer to the 2.75-m-long cell, and the j(2,n) coils to the 1.65-m-long cell. The position refers to the upstream edge of the coil and starts from the beginning of a cell. The radius refers to the inner radius of the coil. The current indices refer to the nomenclature used in the previous table.

Type	Position (m)	Length (m)	Radius (m)	Thickness (m)	j(1,1) (A/mm^2)	j(1,2) (A/mm^2)	j(1,3) (A/mm^2)
Focusing	0.175	0.167	0.330	0.175	75.20	84.17	91.46
Coupling	1.210	0.330	0.770	0.080	98.25	92.42	84.75
Focusing	2.408	0.167	0.330	0.175	75.20	84.17	91.46
					j(2,1)	j(2,2)	j(2,3)
Focusing	0.066	0.145	0.198	0.330	68.87	75.13	83.48
Coupling	0.627	0.396	0.792	0.099	95.65	88.00	76.52
Focusing	1.439	0.145	0.198	0.330	68.87	75.13	83.48

cells, the first as in the previous cells, the second as in the following cells, except that the currents in the central pair of focus coils are set to an average of the currents in the previous and following focusing coils. For instance, Table 5.5 describes the match between the (1,1) and (1,2) lattices.

The match where the cell length changes from 2.75 m down to 1.65 m requires further attention. Although the proposed solution is not a perfect match, its mechanical simplicity and relatively short length may actually outweigh the benefit we might get with a slow, adiabatic match from one cell length to the other. Note that the absorber in the matching cell is removed, allowing us to run the upstream and downstream rf cavity phases closer to the bunching condition and giving us a slight local increase of the rf bucket size, as well as ease of mechanical assembly. Coils and currents are listed in Table 5.6. The magnetic field on axis for the entire cooling channel is shown in Fig. 5.8.

5.3.3.2 Cooling rf

The lengths of the rf cavities are constrained by the lattice design, as the focusing coils have a bore smaller than the rf cavities, and by the rf cell length, which must be optimized to give the high R_S required to reach high gradient (see Chapter 8). In the simulations, cavities are always placed in the middle of the lattice cell. Each rf cell can be phased individually. In order to improve the shunt impedance of the cavity, the iris of the cell

Table 5.5: Geometry and current densities for the solenoids in the first matching section. Coil locations are given with respect to the start of the channel. The coil dimensions are specified in Table 5.4.

Type	Location (m)	j(1,i) (A/mm^2)
	last (1,1)	
Focusing	11.175	75.20
Coupling	12.210	98.25
Focusing	13.408	75.20
	match	
Focusing	13.925	-75.20
Coupling	14.960	-98.25
Focusing	16.158	-80.07
Focusing	16.675	80.07
Coupling	17.710	92.42
Focusing	18.908	84.17
	first (1,2)	
Focusing	19.425	-84.17
Coupling	20.460	-92.42
Focusing	21.658	-84.17

Table 5.6: Geometry and current densities for the solenoids in the matching section between the (1,3) and (2,1) lattices. Coil locations are given with respect to the start of the channel.

Type	Location (m)	Length (m)	Radius (m)	Thickness (m)	j (A/mm^2)
			last (1,3)		
Focusing	41.425	0.167	0.330	0.175	91.46
Coupling	42.460	0.330	0.770	0.080	84.75
Focusing	43.658	0.167	0.330	0.175	91.46
			match		
Focusing	44.175	0.167	0.330	0.175	-91.46
Coupling	45.210	0.330	0.770	0.080	-84.75
Focusing	46.393	0.198	0.330	0.175	-95.24
Focusing	46.816	0.145	0.198	0.330	56.39
Coupling	47.377	0.396	0.792	0.099	95.65
Focusing	48.189	0.145	0.198	0.330	68.87
			first (2,1)		
Focusing	48.466	0.145	0.198	0.330	-68.87
Coupling	49.027	0.396	0.792	0.099	-95.65
Focusing	49.839	0.145	0.198	0.330	-68.87

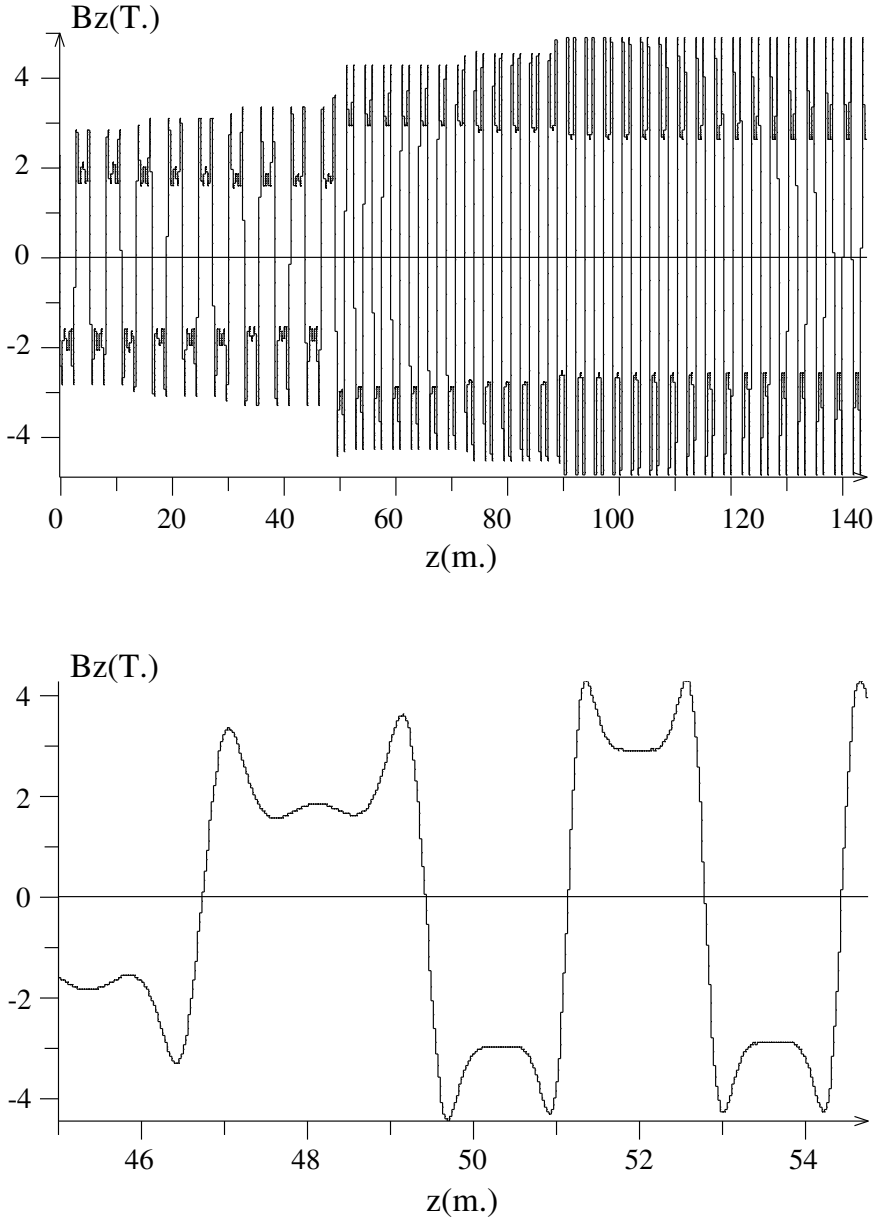

Figure 5.8: B_z on axis for the entire SFOFO cooling channel (top) and for the matching section between the (1,3) and (2,1) lattices (bottom).

is closed with a foil. Our baseline design calls for a thin, pre-stressed beryllium window with thickness that increases with radius. This arrangement is described in Chapter 8. Radius-dependent foil thickness is used because power dissipated in the foil goes like the fourth power of the radius (for small radius). Therefore, we benefit from more thickness at higher radius to remove the heat. In addition, particles at large radius tend to have large transverse amplitude and are "warmer" than the central core. Thus, a bit more multiple scattering can be tolerated at large radius. Windows at the end of a cavity dissipate half as much power as windows at the boundary between two adjacent rf cells. These end windows can be made thinner than those in the center of the cavity. The cavity parameters used in the simulations are listed in Table 5.7. The rf window parameters are in Table 8.5.

Closing the cavity iris with thin aluminum tubes arranged in a Cartesian grid can also be considered, as briefly discussed in Chapter 14.5.

Table 5.7: Geometry and rf parameters for the cavities in the cooling channel used in the simulation study.

Lattice type	No. of rf cells	Cell length (m)	Peak field (MV/m)	Phase (deg.)
(1,i), i=1,3	4	0.466	15.48	40
match	4	0.466	15.48	18.8
(1,3)-(2,1)	2	0.559	16.72	18.8
(2,i), i=1,3	2	0.559	16.72	40

5.3.3.3 Absorbers

The absorber material is liquid hydrogen (LH_2). The LH_2 vessels are equipped with thin aluminum windows; their thicknesses are 360 (220) μm , with radii of 18 (11) cm, for the (1,i) and (2,i) lattices, respectively.

The density of LH_2 is approximately 0.071 g/cm^3. The energy loss, as given by the Bethe-Bloch formula [8] with a mean excitation energy of 21.9 eV, is 4.6 MeV·cm^2/g. The absorber length is 35 cm for the (1,i), i=1,3 lattices and 21 cm for the (2,i) lattices, respectively. The muons lose $\approx$ 12 MeV per lattice cell for the (1,i) lattices and $\approx$ 7 MeV for the (2,i) lattices, including the energy loss in the absorber windows.

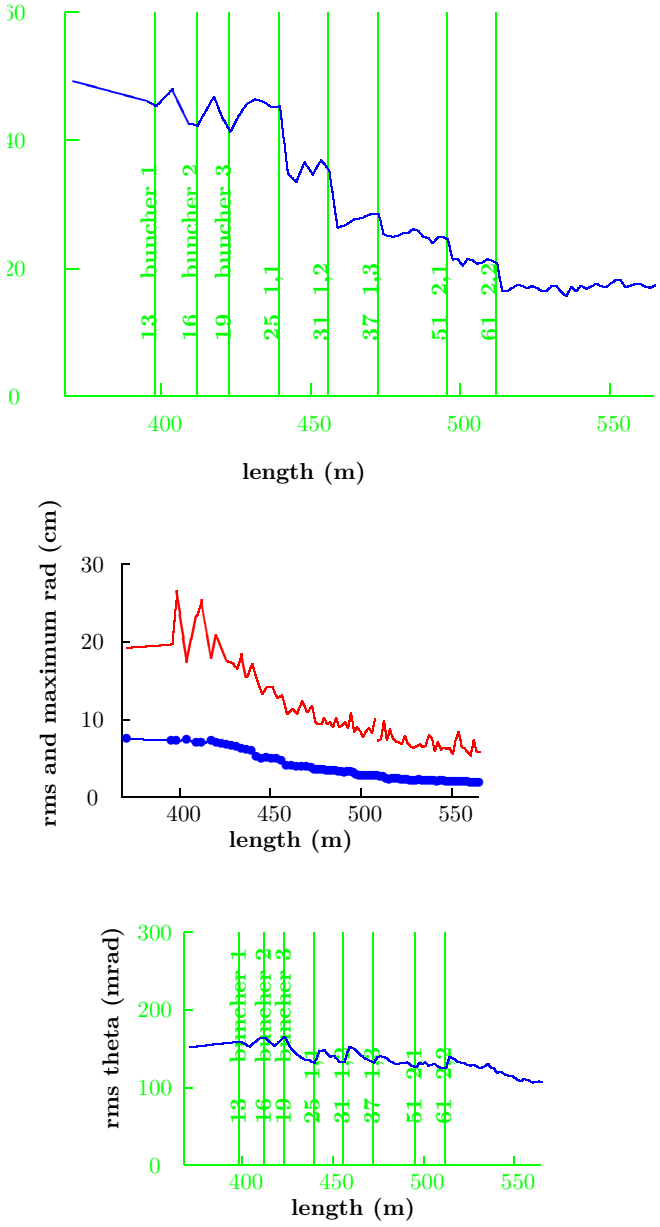

Figure 5.9: Beta function in the buncher and cooling section; rms and maximum beam radius; rms divergence. These results were obtained with ICOOL.

5.3.4 Performance

Fig. 5.9 shows the beta functions, which step down with each new section of the cooling lattice; also shown are the beam radius and beam divergence. The beam divergence at the absorbers is kept approximately constant in order to minimize the effects of multiple scattering. The $\beta_{\perp,min}$ function, derived from the beam second-order moments at the absorber centers, is shown in Fig. 5.10.

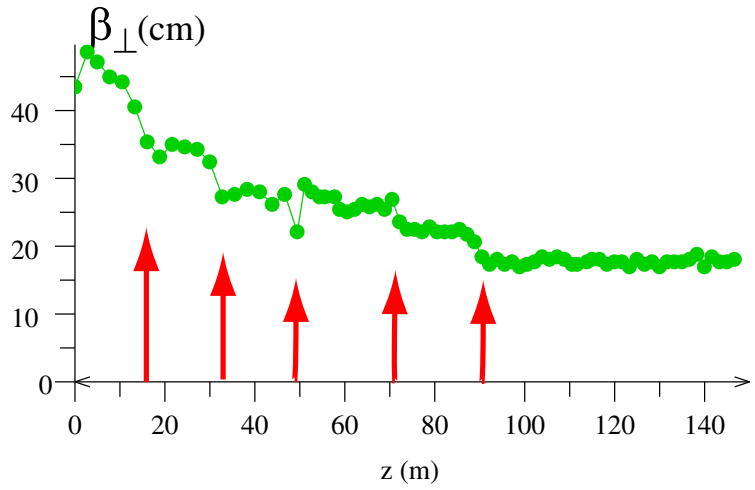

Figure 5.10: The $\beta_\perp$ function for the entire SFOFO cooling channel, averaged over the relevant momentum bite and measured from the second-order moments of the beam itself, as the cooling progresses. The five arrows indicate the beginning of the (1,2), (1,3), and (2,i), i=1,3 lattice sections. (Geant4 result.)

The transverse and longitudinal emittances through the cooling system are shown in Fig. 5.11 and Fig. 5.12. They were obtained using the ICOOL simulation code and the code ECALC9 [9], respectively. Emittances are computed in ECALC9 using diagonalized covariance matrices. These normalized emittance values are corrected for correlations among the variables, including the strong momentum-transverse-amplitude correlation.

The transverse emittance cools from 12 to $\approx$ 2 mm·rad. The longitudinal emittance shows an initial rise, and then, as particles outside the rf bucket are lost, an approach to an asymptotic value set by the bucket size. This longitudinal emittance should naturally rise

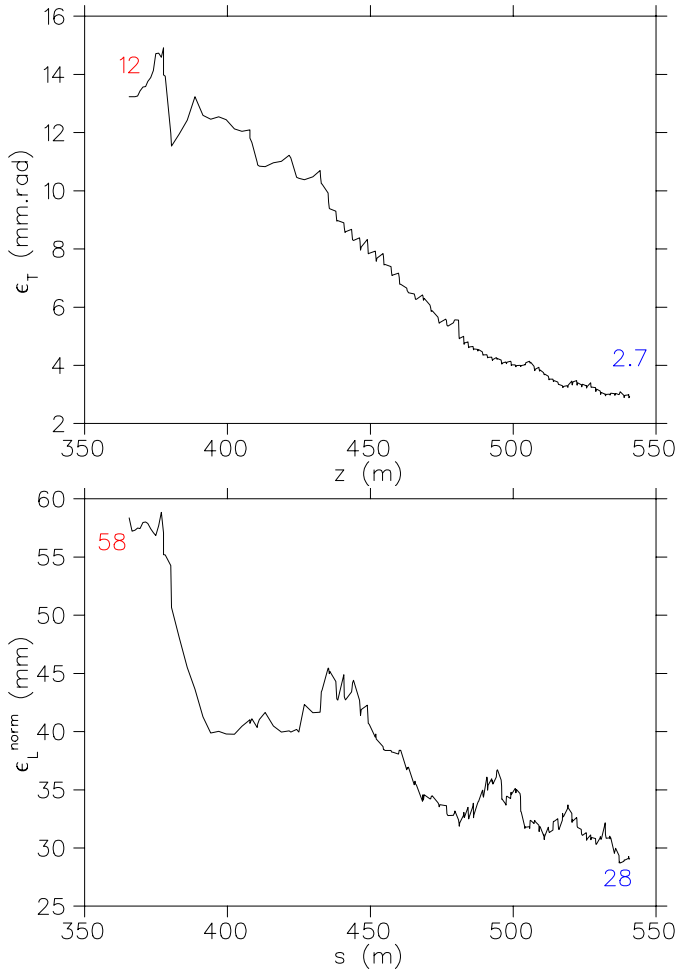

Figure 5.11: Transverse (top) and longitudinal (bottom) emittances in the cooling section, obtained with the ICOOL code. The initial and final values are indicated.

due to straggling and the negative slope of the energy loss curve with energy. However, since the rf bucket is already full, instead of an emittance growth we have a steady loss of particles (*i.e*, "longitudinal scraping"), as seen in the top curve of Fig. 5.13.

Despite this overall loss, the number of particles within the accelerator acceptance increases. The lower two curves in Fig. 5.13 give the number of particles within the baseline longitudinal and transverse acceptance cuts. The middle curve gives the values

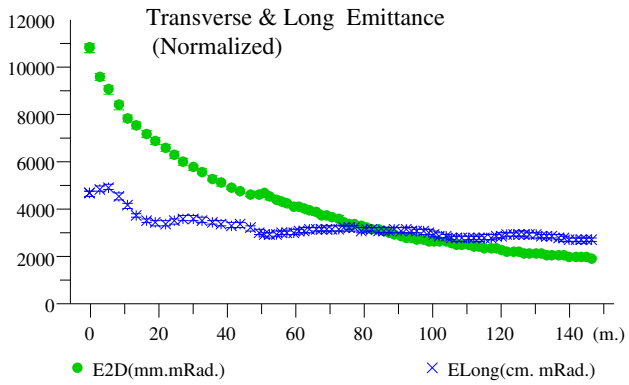

Figure 5.12: The longitudinal and transverse emittances, obtained with the Geant4 simulation code. Notice that the length of the last lattice (2,3), has been extended by ≈ 20 m to investigate the ultimate performance of the cooling channel.

used in this Study (FS2). The lowest curve, shown for comparison, gives the values for the acceptances used in Feasibility Study-I (FS1) [3]. These acceptance cuts are based on the 6D normalized beam emittances derived from the moments of the simulated beam distribution and the estimated transverse and longitudinal beta functions:

- Longitudinal (FS1 & FS2): $(dz^2)/\beta_s \; + \; (dp/p)^2 \; \beta_s \; (\beta\gamma) \; < \; 150 \;$ mm
- Transverse (FS2): $(x^2 + y^2)/\beta_\perp \; + \; (x'^2 + y'^2)\beta_\perp \; (\beta\gamma) \; < \; 15 \;$ mm·rad
- Transverse (FS1): $(x^2 + y^2)/\beta_\perp \; + \; (x'^2 + y'^2)\beta_\perp \; (\beta\gamma) \; < \; 9.35 \;$ mm·rad

where β_s is the synchrotron beta function ($\beta_s = \sigma_z/\sigma_{dp/p}$), and $\beta_\perp$ is the transverse β function. Transverse and longitudinal emittances obtained with Geant4 are shown in Fig. 5.12. At equilibrium, a transverse emittance of 2.2 mm·rad is reached, consistent with the ICOOL result.

It is seen that the gain in muons due to cooling within the accelerator acceptance is a factor of ≈ 3 (or ≈ 4 if the Study-I acceptances were used). Similar performance is obtained with the Geant4 code, as shown in Fig. 5.14. If the particle loss from longitudinal emittance growth could be eliminated, as might be the case if emittance exchange were used, then these gains might double.

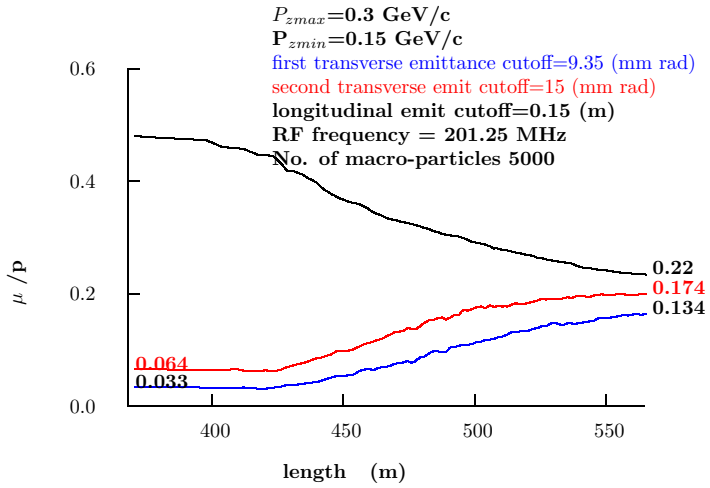

Figure 5.13: Particle transmission: number of muons per incident proton on target in the buncher and cooling sections. Top curve is overall transmission; lower two curves are for 150 mm longitudinal acceptance with two different transverse acceptance cuts: (middle) 15 mm·rad transverse acceptance; (bottom) 9.35 mm·rad transverse acceptance. This result was obtained with ICOOL.

The beam characteristics in the buncher and cooling sections are summarized in Table 5.8. This table lists the properties of all the muons in the beam that survive to a given location. The beam is cylindrically symmetric in this lattice, so the x and y properties are similar. We see that the beam size steadily decreases as we proceed down the channel. The angular divergence is kept approximately constant, maximizing cooling efficiency. The momentum spread of the entire beam is still large after the induction linac, but this includes very low and very high energy muons that do not get transmitted through the subsequent SFOFO lattice. For example, the range of momenta accepted in the acceleration linac is 150–300 MeV/c. The rms momentum spread for muons that lie inside this momentum range varies from 16 MeV/c after the third induction linac to 21 MeV/c after the 1.65 m cooling lattice.

The decrease in energy spread shown in Table 5.8 is due to particle losses, since there is no longitudinal cooling or emittance exchange. Likewise, the average momentum of the

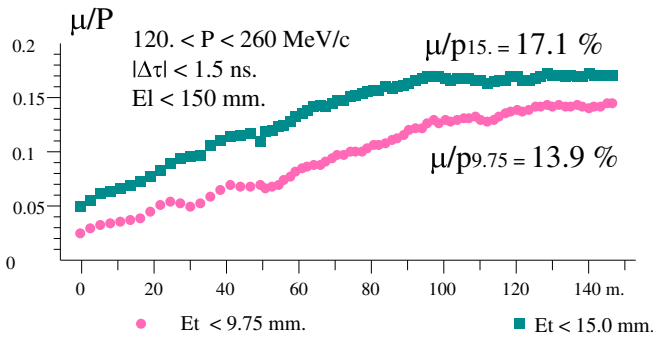

Figure 5.14: The muon-to-proton yield ratio for the two transverse emittance cuts, clearly showing that the channel cools, *i.e.*, the density in the center of the phase space region increases. Since the relevant yield μ/p_{15} no longer increases for $z \leq 110$ m, the channel length was set to 108 m. This is a Geant4 result.

Table 5.8: Beam characteristics summary.

Location (end of)	σ_x (cm)	$\sigma_{x'}$ (mrad)	σ_p (MeV/c)	σ_t (ns)	$\langle p \rangle$ (MeV/c)
Induction linac	8.6	95	118		237
Matching section	5.8	114	115		247
Buncher	5.1	104	101	0.84	238
2.75 m cooler	3.0	89	64	0.55	219
1.65 m cooler	1.6	94	28	0.51	207

beam decreases until it matches the acceptance of the SFOFO lattice. The time spread refers to a single bunch in the bunch train.

The longitudinal emittance remains more or less stable, at around 30 mm. This is somewhat deceptive. The anti-damping slope of the energy loss curve, straggling, and imperfections in the longitudinal-to-transverse correlation[1] cause particles to fall out of the rf bucket and be scraped away due to the strong betatron resonances. In fact, the buncher delivers a full rf bucket to the cooling section and the longitudinal emittance cannot grow any larger. This scraping occurs on the combined time scales of the synchrotron period, about 20 m, and the growth time of the betatron resonance instability.

The performance of the cooling channel is influenced by both multiple scattering and the limited momentum acceptance. Without multiple scattering, the μ/p_{15} and $\mu/p_{9.35}$ yields would increase by approximately 20% and 40%, respectively.

5.3.5 Tolerances & Systematics

The performance of the cooling channel has been evaluated based on computer simulations using two distinct codes. However, some parameters or assumptions in the calculations are common in the two simulations. Since no such channel has been built yet, it is fair to question whether the estimation of the cooling performance is robust against small changes in these parameter values. In addition, we need to consider the tolerances on the mechanical alignment in such a long beam transport system.

5.3.5.1 Sensitivity to multiple scattering model

ICOOL treats multiple scattering by using a straightforward Moliere model, imported from the Geant3 package. Geant4 uses an improved version of the Moliere model, but has a tunable parameter. We have studied the sensitivity of the rms value of the scattering angle to this parameter, in relation to the known uncertainties in the measured values for these rms scattering angles for low-Z materials. The sensitivity of the μ/P_{15} yield in the relevant range of this tunable parameter has been measured. The systematic error due to this uncertainty is approximately 10%.

5.3.5.2 Control of the energy loss in LH_2 and energy gain in the linac

Because of the relatively narrow momentum acceptance of the channel compared with the beam momentum spread, the energy loss and the energy gain must be known in the

[1] See Fig. 5.4 in the previous section.

channel to better than $\approx 0.25\%$. This tolerance can be achieved in the rf cavities, where the peak voltage and accelerating voltage can be controlled to better than a few tenths of a percent.

Nonuniform heat deposition within the absorbers may cause density variations in the vicinity of the core of the beam. These could result in reduced beam cooling as well as a net acceleration of the beam through the cooling channel, since the reduced energy loss would then be overcompensated by the rf accelerating gradient. While the absorber R&D program has not yet reached the point where such variations may be predicted in detail, we believe that they will be small in view of the success of the SAMPLE collaboration at Bates Laboratory in maintaining constant target density within tenths of a percent with 500 W of beam heating [20].

We have also explored, by simulation, the effects on muon cooling performance of reduced absorber density. As a first approximation the absorber density has been reduced uniformly throughout all absorbers by 1, 3, 5, 10, and 20%. For density decreases up to 5%, the cooling performance is unaffected within the few-percent level of simulation statistics.

The cooling channel will require about 72 12-MW klystrons. It is likely that one will fail occasionally. If so, emptying an LH_2 vessel and rephasing the downstream rf cavities will keep the beam on the nominal momentum. As an example, we have simulated the loss of rf power in a (1,1) or a (1,3) cooling cell. We find that emptying the absorber vessel and rephasing the remaining rf cavities results in a performance degradation of about 5% (relative), allowing us to keep the cooling channel running productively.

5.3.5.3 Magnet alignment

The design of the cooling channel was optimized using ideal magnetic fields from cylindrical current sheets. In an actual magnetic channel, imperfections that occur in the fabrication and assembly of the solenoids result in magnetic fields that deviate from the ideal used in the simulations by some small error field $\delta\vec{B}(x, y, z)$. A state-of-the-art magnet construction results in field errors $\frac{\delta B}{B} \leq 0.1\%$. These field errors produce effects, in general detrimental, that tend to increase with the length of the channel. If left uncorrected, these errors lead to mismatching and betatron oscillations, which in turn result in degradation of the cooling performance of the channel and to a decrease of the channel transmission.

We have considered the following analytical treatment of the detrimental effects of magnet alignment errors. As the muon beam propagates along the periodic channel with a prescribed beta function, it encounters a series of errors of various origins, which are assumed to be described by a stochastic function $\delta\vec{B(s)}$ (we neglect the transverse

coordinate dependence). The muons experience a series of random forces or "kicks," which result in a random walk of the centroid of the beam. Statistically, the rms magnitude of the transverse deviation $\sqrt{<(\delta x(s))^2>}$ is a function of the length of the channel, s. In principle, it should be possible to develop a correction algorithm such that strategically located correction coils bring the centroid back to the ideal trajectory, thereby minimizing the deterioration of the cooling process.

A first look at the effects of errors and the sensitivity of the present design of the cooling channel to them has been carried out in references [10] and [11]. Studies of the error fields due to misalignment of individual coils and current sheets are found in references [12],[13].

There are several sources of magnet imperfections that may contribute to the overall deviation from the ideal fields of the channel:

1. Geometric (*macroscopic*) survey errors:

   a) transverse misalignment of solenoids, characterized by a vector $\vec{d} = \vec{d}\,(\cos\theta, \sin\theta, 0)$ of magnitude d and direction θ. In the simulations the values of d are chosen from a Gaussian stochastic function.

   b) transverse tilt of the solenoid, characterized by two angles: θ direction with respect to the x-axis, and the tilt, by the magnitude ψ, with respect to the z-axis.

   The Cartesian coordinates $\vec{r} = (x, y, s)$ transform as

$$\vec{r'} = \vec{r} - \vec{d} \tag{5.6}$$

   for a translation in the transverse plane and

$$x'_i = \mathcal{M}_{ij} x_j \tag{5.7}$$

   for a tilted magnet. The magnetic fields are calculated as

$$\vec{B}(x, y, s) = \vec{B'}(x', y, s') \qquad B_i(\vec{r}) = \mathcal{M}^{-1}_{ij} B'_j(\mathcal{M}\vec{r}) \tag{5.8}$$

   for a translation and tilt respectively. The transformation matrix is

$$\mathcal{M} = \begin{bmatrix} \cos\psi + \cos^2\theta(1-\cos\psi) & \sin\theta\cos\theta(1-\cos\psi) & \sin\theta\sin\psi \\ \sin\theta\cos\theta(1-\cos\psi) & \cos\psi + \sin^2\theta(1-\cos\psi) & \cos\theta\sin\psi \\ \sin\theta\sin\psi & -\cos\theta\sin\psi & \cos\psi \end{bmatrix} \tag{5.9}$$

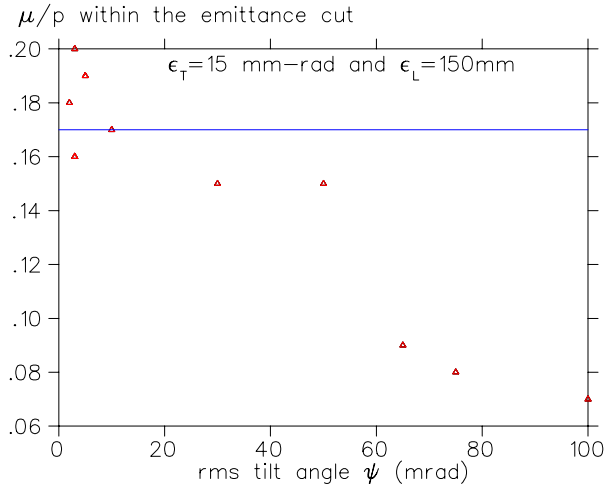

Figure 5.15: Transmission of the front end for different *rms* tilt angles.

2. Power supply fluctuations resulting in current fluctuations

3. Geometric conductor positioning, which leads to random *microscopic* field errors.

Here we only consider the first type, *i.e.*, geometric *macroscopic* field errors introduced by mispositioning of entire magnet cryostats.

We have performed two studies with ICOOL [1]. The buncher and SFOFO cooling channel have been simulated with independent Gaussian random tilt angles and translation of the coils roughly every 5 m. The results are shown in Figs. 5.15 and 5.16.

An independent analysis of alignment tolerance issues (microscopic field errors) has been done using the Geant4 package. The simulations of the buncher and cooling channels are run in the following modes:

1. Random polar tilts. A Gaussian model was used to generate the tilts, polar angles ψ, for each coil. Since large transverse displacements of coils are expected to be relatively easy to find and correct, we have truncated the distribution at $2\sigma_\psi$. The azimuthal θ angles were chosen randomly, between zero and 2π. The μ/p_{15} yield was measured for tens of such simulated channel assemblies. The histogram in Fig. 5.17 shows that a σ_ψ of 0.5 mrad gives no statistically significant degradation of the channel performance. However $\sigma_\psi \approx 2.5$ mrad would be unacceptable.

2. Random transverse displacements. Since the coils are about 15 cm long, a tilt of 0.5 mrad gives a lateral displacement at one end of about 75 μm. Evidently, the coil

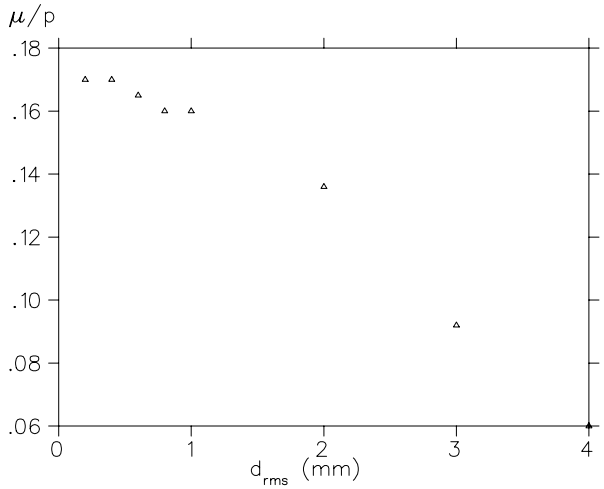

Figure 5.16: Transmission of the front end for different rms translation errors d.

could also shift laterally by about the same amount. We verified that a 2σ truncated displacement of 100 μm has no significant impact on the channel performance.

Since the typical tolerance on accelerator magnet alignment is about 100–μm, we believe that such a channel can be assembled to the required accuracy.

5.3.5.4 Space charge

The nominal number of muons per bunch is $N_\mu \approx 5{\times}10^{10}$, which corresponds to $Q \approx 8$ nC. An estimate of the deleterious effect of space charge on the beam dynamics can be found by calculating the self-electric field of a Gaussian distribution of charge represented by the Basetti-Erskine-Kheifets formula [14]

$$\Phi(r,z,s) = \frac{2Q}{\epsilon_o\sqrt{\pi}} \int_0^\infty dt \frac{e^{-\frac{r^2}{2{\sigma_\perp}^2+t}}}{(2{\sigma_\perp}^2+t)} \frac{e^{-\frac{z^2}{2{\sigma_3}^2+t}}}{\sqrt{(2{\sigma_3}^2+t)}}. \tag{5.10}$$

The variable z is defined as $z = s - c\beta t$, with s the longitudinal coordinate, assuming that the centroid of the bunch is at $s = 0$ at time $t = 0$. The argument s in $\Phi(r,z,s)$ is there to indicate that the rms transverse size $\sigma_\perp$ and longitudinal size σ_z of the beam are functions of s. This is important because the beta function varies from moderate to small values at the absorbers.

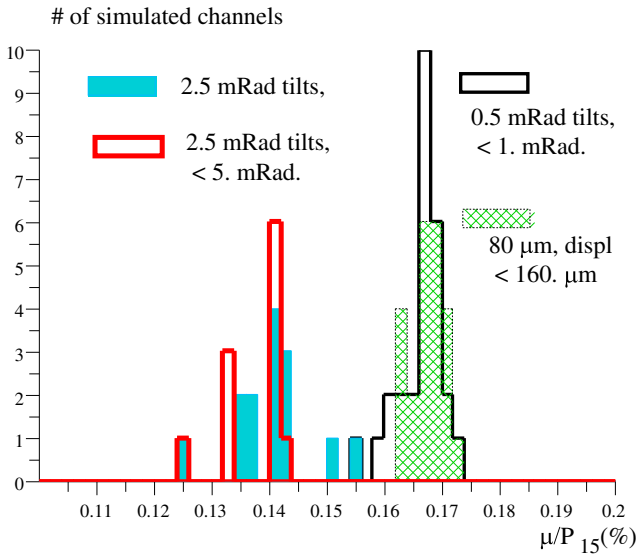

Figure 5.17: A histogram of the performance of 35 SFOFO cooling channels built with tolerances of 0.5 and 2.5 mrad tilts and small translations.

From Eq. 5.10 and the corresponding expression for the vector potential $A_s(r,z,s) = \beta\Phi(r,z,s)$ we can calculate the electric field components $E_r(r,s,t)$ and $E_s(r,s,t)$ [15]. ICOOL contains this formulation and systematic studies have been carried out. The results are shown in Fig. 5.18, where it can be seen that the number of muons per proton μ/p at the end of the cooling channel is rather insensitive to the number of muons in the bunch up to values $N_\mu^{critical} \approx 1 \times 10^{12}$, some 20 times our intensity.

This approach is approximate and leaves aside potentially important phenomena: first, the effects of induced charge in the walls of the beam pipe and in the metallic (Be) rf windows; second, the short-range wake potential created by the $\beta < 1$ muon beam inside the cavities. The effect of the walls of a cylindrical beam pipe on a bunch of charged particles was also considered and has been computed with ICOOL with no noticeable effects. We note here that the presence of Be windows should mitigate any space charge effects. However, it is rather difficult to calculate this with precision.

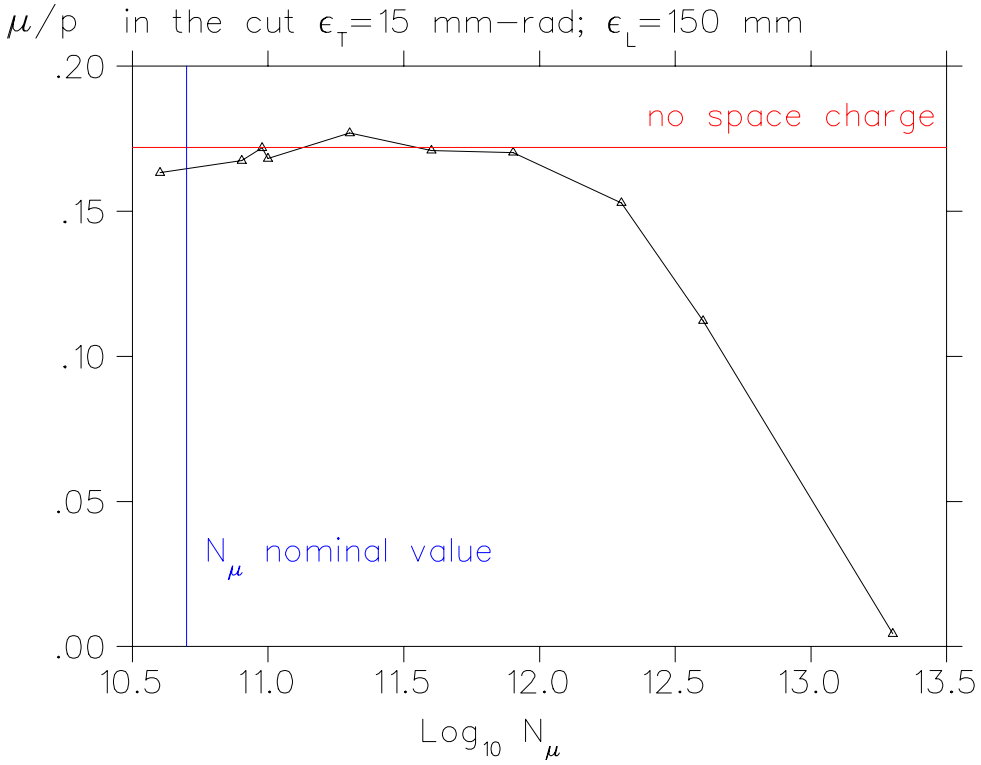

Figure 5.18: μ/p *vs.* N_μ in a bunch, assuming a Gaussian self-field.

5.3.6 Liquid Hydrogen Absorbers

5.3.6.1 Power handling

We estimate the maximum power dissipation per absorber to be about 300 W, dominated by the ionization energy loss of the muons (See Table 4.4, which shows the absorber lengths, radii and the number of absorbers of each type). The main technical challenge in the absorber design is to prevent boiling of the hydrogen near the beam axis, where the power density is greatest. This requires that the hydrogen flow have a significant component transverse to the beam. We are investigating two ways to achieve this: "flow-through", a design in which the absorber connects to an external heat-exchange and temperature-control loop, and "convection", a design in which the absorber vessel is itself the heat exchanger, and heat transfer within the absorber is accomplished dominantly by convection.

The flow-through design resembles previous high-power liquid-hydrogen targets [19, 20], which have been operated successfully at power dissipations as high as 500 W [20] and have been proposed for operation at even higher dissipations [21, 22]. In this approach the hydrogen is pumped around a loop that includes the absorber vessel, as well as a heat exchanger and a heater. In the heat exchanger, which runs at a constant power level, the hydrogen is cooled by counterflowing cold helium gas. The heater is used in feedback to regulate the hydrogen temperature and compensate for changes in beam intensity.

Given the small emittance of conventional particle beams, liquid-hydrogen targets tend to be narrow transverse to the beam, leading to designs in which the natural direction of hydrogen flow is parallel to the beam. To avoid boiling the liquid in the high-intensity beam core, various design strategies are then necessary to ensure transverse flow of the liquid [20, 23]. In contrast, in our flow-through design the hydrogen enters the absorber vessel from below and exits at the top, ensuring automatically that the flow is transverse to the beam. The flow pattern is controlled by means of nozzles, which must be configured so as to avoid dead regions or eddies and to ensure adequate flushing of the windows.

In the convection design (Fig. 5.19), the interior wall of the vessel is equipped with cooling tubes through which cold helium gas circulates. A heater located at the bottom of the vessel is used to compensate for changes in beam intensity. The design of the convection-cooled absorber is being guided by two-dimensional fluid-flow calculations. The flow-through approach is less amenable to calculation, but will be tested on the bench to verify the efficacy of the nozzle design, first in a room-temperature model and later at cryogenic temperature. Prototype construction and testing programs for both designs are now under way and will lead to high-power beam tests.

5.3.6.2 Window design

To minimize heating of the beam due to multiple scattering, the absorbers must be equipped with thin, low-Z windows. Yet, the windows must be strong enough to withstand the pressure of the liquid hydrogen. We have devised a window design that satisfies these requirements and also allows quite thin absorbers to be built. While a hemispherical window shape minimizes the window thickness for a given strength, the desire to build absorbers that are thinner relative to their diameter than a sphere leads to the "torispherical" shape. In the version specified by the American Society of Mechanical Engineers (ASME) [24], the torispherical head for pressure vessels is composed of a central portion having a radius of curvature (the "crown radius") equal to the diameter of the cylindrical portion of the vessel, joined to the cylindrical portion by a section of a toroidal surface with a radius of curvature 6% of the crown radius (see Fig. 5.20).

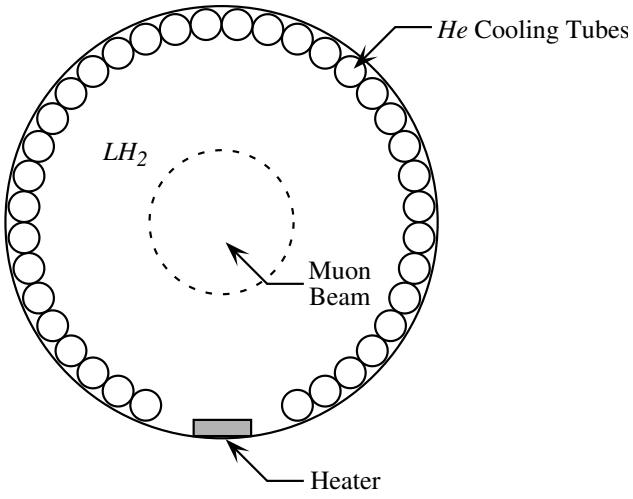

Figure 5.19: Schematic of convection design.

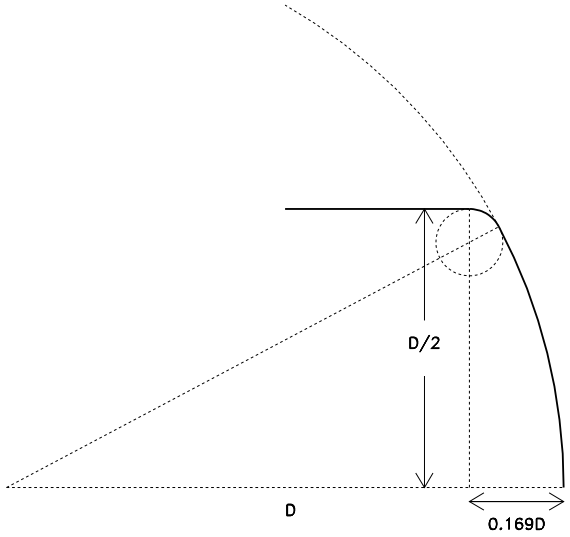

Figure 5.20: Schematic of ASME torispherical head on cylindrical vessel of diameter D: solid curve shows upper half section, with dashed lines and curves indicating the spherical and toric surfaces from which it is composed.

ASME specifies the minimum acceptable thickness of the torispherical head as

$$t = \frac{0.885PD}{SE - 0.1P}\,, \tag{5.11}$$

where P is the differential pressure across the window, D the vessel diameter, S the maximum allowable stress, and E the weld efficiency. Although previous high-power liquid-hydrogen targets have operated at 2 atm [19, 20], to keep the windows as thin as possible we have designed for 1.2 atm. For S, we follow ASME recommendations and use the smaller of 1/4 of the ultimate strength S_u or 2/3 of the yield strength S_y (in practice, for aluminum alloys it is the ultimate strength that matters). We will machine the window with an integral flange out of a single disk of material (Fig. 5.21), with the flange fastened to the assembly by bolts (Fig. 5.22). Thus, there are no welds and we take $E = 1$. For 1.2-atm operation, and given the ASME specification for 6061-T6 aluminum alloy, $S_u = 289\,\mathrm{MPa}$, we obtain $t = 530\,\mu\mathrm{m}$ for the "Lattice 1" absorbers ($D = 0.36\,\mathrm{m}$) and $t = 330\,\mu\mathrm{m}$ for the "Lattice 2" absorbers ($D = 0.22\,\mathrm{m}$). If necessary, the windows can be made thinner than this by tapering their thickness as described below. In addition, less easily machinable, but stronger, aluminum alloys (such as 2090-T81) may allow further reduction in thickness.

In addition to eliminating the weld, machining the window out of a single disk allows detailed control of the window shape and thickness profile. We have used the ANSYS finite-element-analysis program to optimize the window shape and profile so as to minimize the window's thickness in its central portion, where most of the muons traverse it. The resulting shape and thickness profile are shown in Fig. 5.21. Therefore we have used in the simulation the smaller thicknesses of 360 μm and 220 μm for the (1,i) and (2,i) cooling lattices, respectively.

5.3.7 Diagnostics and Instrumentation Issues in the Cooling Channel

There are a number of unique instrumentation problems involved in optimizing and monitoring the performance of the cooling line [25]. The beams will be large and intense, and a variety of precise measurements will be required that are both novel and difficult.

There will be significant backgrounds in all detectors, due either to other particles from the target coming down the line with the muons, or to x-rays and dark currents generated by the rf cavities. We must consider the angular momentum of the beam, perhaps for the first time with any high energy physics beam. The beams will be intense enough so that thermal heating of the detectors is significant. The environment will have high magnetic fields, a large range of temperatures, and high-power rf cavities. In addition, under normal circumstances the access will be very limited, since the rf cavities and liquid hydrogen absorbers will occupy most of the available space. Standard loss monitors will not be useful for the low energy muons because the range of such particles

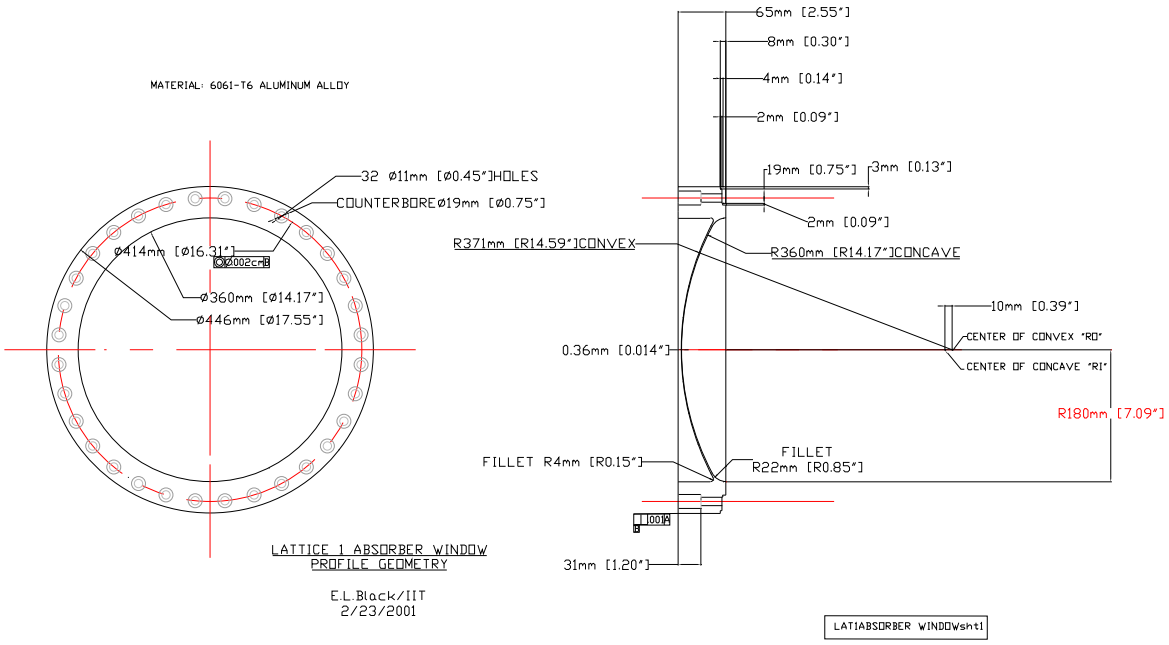

Figure 5.21: Window design for the SFOFO Lattice 1 absorbers.

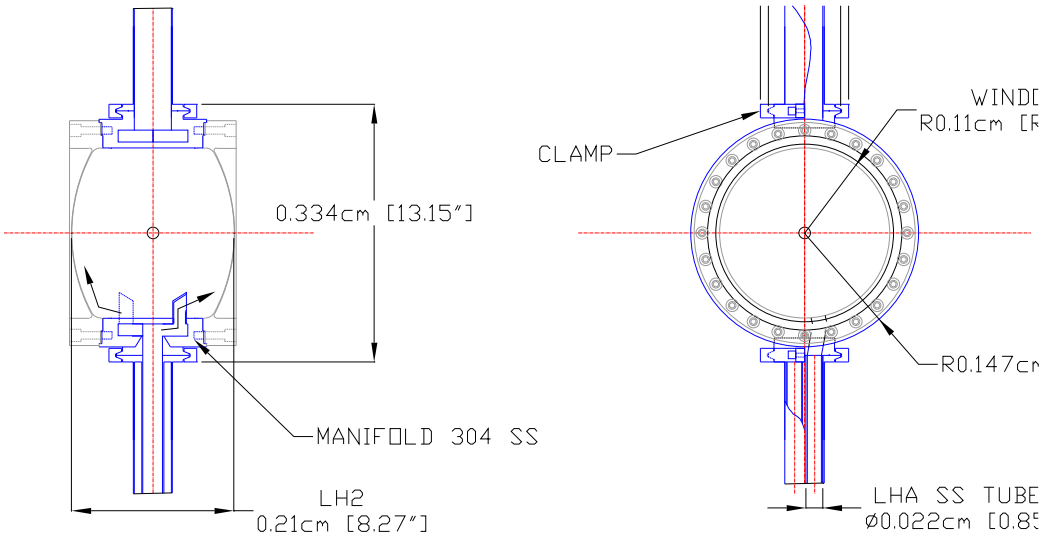

Figure 5.22: Absorber assembly for SFOFO lattice 2 (flow-through design shown).

is so short (6 cm in Cu) and they produce no secondaries. An R&D program is under way to look at the sensitivity and usefulness of different diagnostic techniques and evaluate them in the environment of rf backgrounds and high magnetic fields.

On the other hand, there are a number of reasons why the tune-up and operation of the cooling channel could be fairly straightforward. The cooling channel will have been very thoroughly simulated by the time of initial construction. In addition, there are a relatively small number of variables that control the behavior of the beam, such as currents in solenoids, rf parameters and liquid-hydrogen-absorber parameters, and these can be measured with high precision. While the change in transverse beam emittance, $\epsilon_\perp$, between individual cells may be difficult to measure, $\Delta\epsilon_\perp/\epsilon_\perp < 0.01$, the overall size and profile of a beam with $\sim 10^{12}$ particles per macro-bunch is a comparatively straightforward measurement.

5.3.7.1 Measurement precision

The sensitivity of the system to alignment errors was described in Section 5.3.5. Related issues involve sensitivity to various other effects: transverse and longitudinal mismatches between the cooling line and the bunching section, arc-down and temporary loss of an

rf cavity, boiling or loss of hydrogen in the absorber section, inadvertent introduction of a collimator or thick diagnostic, and mismatches at the ends of the cooling line. These mismatches can be either first-order (beam centroid position, energy, or angle errors), or second-order (discontinuities in Twiss parameters). Mismatches will slow down the cooling process and could significantly affect beam losses.

A mismatch due to problems with the rf or absorbers would change both the mean beam momentum and the measured β function downstream. An example is shown in Fig. 5.23, where the beta functions are plotted through regions where the momentum has changed, corresponding to an empty hydrogen cell or a single rf cavity that is turned off, giving the scale of the effects that might be produced. The changes in β functions are a few percent at some positions, while at other points the β functions are essentially unchanged. Thus, it is necessary to have beam profile measurements done at a number of positions. Mismatches in the beam optics would persist until chromatic effects caused decoherence of

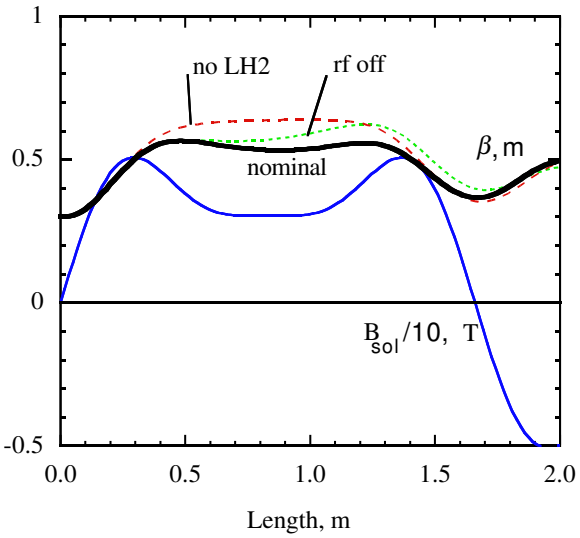

Figure 5.23: The scale of discontinuities in β function when rf or absorbers are perturbed, corresponding to empty liquid-hydrogen absorber (dashed line) or shorted rf cavity (dotted line).

the betatron motion (and perhaps subsequent recoherence due to synchrotron motion). The ultimate emittance growth, due to filamentation, would be of the same order of magnitude as the change in β functions. If a change in momentum persisted through the

end of the cooling line, it could be detected in dispersive areas of the beam transfer lines, but the synchrotron motion could cancel the energy fluctuation. Thus, it is desirable to diagnose the beam using the transverse optics.

An R&D program is under way to look at the sensitivity and usefulness of different diagnostic techniques and evaluate them in the environment of rf backgrounds and high magnetic fields. Modeling is also required to understand mismatches and realistic errors better.

5.3.7.2 Angular momentum

Angular momentum plays an important role in solenoidal ionization cooling channels, unlike the quadrupole channels commonly used elsewhere in high energy physics. Due to the rotational symmetry of the solenoid focusing field, the canonical angular momentum is a conserved quantity when the cooling material is absent. When absorbers are present, however, the beam angular momentum can change, thereby yielding a residual angular momentum at the end of a cooling channel. Non-zero beam angular momentum creates coupling between the two transverse degrees of freedom and causes problems for matching the beam into a downstream quadrupole channel. Furthermore, the angular momentum intrinsically couples with the beam emittance in the cooling dynamics. For optimum cooling in a periodic channel, the change in the net angular momentum should be zero. This requirement becomes the following condition [26]

$$\int_0^\lambda \eta(s)\beta_\perp(s)B(s)ds \sim 0 \tag{5.12}$$

where λ is one period, $B(s)$ is the on-axis magnetic field, $\beta_\perp(s)$ is the envelope function, and $\eta(s)$ is the ionization energy loss rate.

Measurement of beam angular momentum is a new subject. Beam profile monitors, which measure beam distributions in x and y, can measure the beam emittance, but do not provide sufficient information to directly determine the angular momentum in a solenoid cooling channel. We are investigating whether it is possible to indirectly measure the angular momentum by comparing the measured emittance-damping rates. Clearly, such measurements will be difficult. Novel ideas are being explored to directly measure the correlation terms $\langle xp_y \rangle$ [27].

Since the energy loss rate, absorber thickness, and magnetic field are known, or can be measured with an accuracy much better than one percent, and an envelope function measurement is likely to be accurate to a few percent, it should be possible to determine whether Eq. 5.12 is approximately satisfied. For machine operation purposes, beam angular momentum measurements are helpful, but not absolutely necessary.

5.3.7.3 Backgrounds

There are a number of backgrounds that will impact beam diagnostics. These backgrounds come primarily from three sources: 1) backgrounds produced by the incident protons at the target; 2) backgrounds produced in the cooling line, primarily from rf cavities; and 3) backgrounds from decay electrons. We assume that the decay electrons can be simulated and subtracted from all measurements.

5.3.7.3.1 Beam backgrounds The solenoidal beam transport channel for muons will also transport all other particles whose transverse momentum is less than ∼100 MeV/c. Thus, hadronic showers from 3 GeV protons, for example, can be expected in the liquid hydrogen absorbers well down the cooling line. A large number of species are produced: K, n, γ, $e^{\pm}$, D, He^3, He^4, and other nuclear fragments should be seen in detectable quantities. Most low-energy backgrounds from the target will be stopped in the first minicooling absorber, but the high energy particles that are left will be comparatively unaffected by the rf in the line. Timing should be very effective in identifying and discriminating against these particles.

5.3.7.3.2 RF backgrounds X-ray production from rf cavities results from dark-current electrons hitting the body of the cavity and nearby solid components. The bremsstrahlung x-ray flux produced is then scattered and attenuated by both the production material and by transmission through any external structure. While the dark-current electron orbits will be influenced by magnetic fields along the beam axis, the x-rays, particularly those around 1-2 MeV, will scatter and diffuse freely up and down the cooling line. The dark-current electrons from single-cell cavities, and the x-rays they produce, are expected to be in the 1–10 MeV range. The electron and x-ray fluxes produced in this environment have recently been measured using a 1.3 GHz high-gradient cavity [28]. Other experiments are planned using an 805 MHz cavity. Data taken from a variety of pulsed cavities suggest that rf breakdown limits the total dark current, and thus the x-ray flux that can be produced, somewhat independent of frequency.

Fluxes of dark-current electrons and x-rays measured in the 1.3-GHz cavity were on the order of 10^{10}–10^{11} electrons per rf pulse, or 10^7 – 10^8 electrons per bucket, a more relevant parameter. The number of bremsstrahlung photons is of the order of $n_e r/L_R$ where n_e is the number of dark-current electrons, r is their range, usually a few mm, and L_R is the radiation length for the material, *e.g.*, 1.44 cm for Cu. Because the energies are low, complex showers do not develop. The photons, however, do diffuse through the system.

There are several ways of altering the flux of dark-current electrons and the x-ray flux seen by the beam diagnostics:

- the geometry of the system can be changed so that dark-current electrons do not appear near the beam axis (the double-flip cooling channel option described in Section B does this, because the rf cavities are inside of a uniform solenoidal field and, consequently, it is less likely that dark-current electrons will be guided into the diagnostic device)
- rf electric field, E_{rf}, can be reduced since $I_{dark} \propto E_{rf}^{10}$
- cavity can be coated with a material having low secondary electron yield.

All of these methods are to some extent applicable to the cooling line.

5.3.7.4 Access in the cooling line

It is desirable to be able to insert, park, and possibly remove any instrumentation in the line without disrupting the beam vacuum. There are a number of options for insertion of diagnostics into the cooling line.

Analogous to FODO accelerator structures, it is desirable to insert diagnostics at every major focusing element. While there is limited space in the cooling line, instrumentation modules compatible with the 3.7 cm expansion section that is a part of every cell can be used. Figure 5.24 shows a possible location for inserting diagnostics in the cooling cell.

Special SFOFO sections, without hydrogen absorbers and with only enough rf voltage to contain the bunch, could also be used for specific Cherenkov counters or other devices that require more access than would be available in a standard cell. We have not made use of this concept as part of this Study, but it is compatible with the cooling channel.

5.3.7.5 Making and using pencil beams

We anticipate that pencil beams will be very useful in assessing the alignment of all cooling, accelerator, and storage ring components. Since the range of the roughly 200 MeV/c muons in the cooling line is only about 6 cm in Cu, and scattering angles are large, collimation works very well. Thus a variety of collimators could be used at locations in the bunching and cooling lines to produce low transverse emittance beams, on or off axis.

Producing a 6D "pencil" may be even more useful, since this could be used to track the longitudinal evolution of the bunch through all of the acceleration and storage ring optics. In principle, the 6D bunch can be produced from a 4D bunch by reducing the rf voltage in the cooling line, so that only the center of the longitudinal phase space is

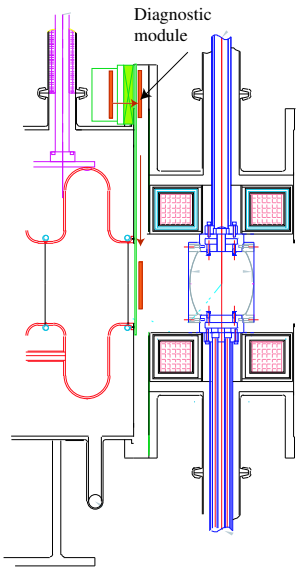

Figure 5.24: Possible location for diagnostic instrumentation in a standard cooling lattice cell. The arrows show how a diagnostic module could be removed from its parked position and inserted into the beam temporarily for measurements.

transmitted. While the intensities will be reduced, muon beams in the range of 10^{10} to 10^{11} particles should be useful and quite easily measured.

5.3.7.6 Instrumentation options

Although high-energy particles, dark-current electrons and x-rays will be present, the signal from the primary muon beam should dominate these backgrounds. Nonetheless, we will look first at instrumentation options that offer very fast time response; these will be relatively less sensitive to backgrounds. From this perspective, segmented secondary emission monitors (SSEMs) and Faraday cups offer a significant advantage. These devices have been shown to have a useful resolution time of the order of 150 – 200 ps. Since this time response is significantly less than the bucket length, these devices would be able to provide some information on the bunch shape and thus on the longitudinal emittance of the beam. Faraday cups could be used essentially interchangeably with the SSEMs. However, they would provide about two orders of magnitude more dynamic range, and the possibility of some particle discrimination using range.

These devices can be used both to measure the beam parameters, and to provide consistency checks for evaluating measurements by other methods. One possibility being considered is a curtain of scintillating fibers, with an actuator to slide the fibers into place when beam diagnostics are needed and a safe parked area out of the way during normal operating conditions. Likewise, a telescoping 2D pixel-array SEM is envisioned that can be inserted to diagnose the center or edge of the beam region.

It is possible that detectable scintillation may occur when the muon beam passes through the liquid-hydrogen absorbers. If this is verified in cosmic-ray tests, it would provide a diagnostic that is always present and does not add any additional material in the beam. The scintillation should provide a signal with good time resolution and 2D position information.

Semiconductor arrays of polycrystalline CdTe would be able to provide high-precision x and y beam profiles in a single measurement [29]. The detector consists of an array of charge-sensitive elements, each providing a signal with amplitude proportional to the intercepted muon beam density. Finally, bolometers are being developed that can measure xy profiles from the heating in the metallic windows of the liquid-hydrogen absorbers. We are also looking at high-rate ion chambers, which would be generally useful for a wide range of measurements. Tests of how these various devices perform in the high x-ray-flux environment of a cooling channel will be done as part of the R&D program.

5.3.8 Engineering Considerations

The fully-integrated layout of the cooling cells for the (1,i) lattices and the (2,i) lattices are shown in Figs. 5.26 and 5.25.

This design takes into account the constraints from the solenoid magnet subsystem (see Figs. 5.27, 5.28 and 10.6) described in Chapter 10, the rf cavities discussed in Chapter 8, and the absorber detailed in Section 5.3.6. The basic dimensions of the cooling cells are taken from the conceptual design presented above. However, the exact placement of various components may depart slightly from the layout used in the simulation package. For instance, the rf cavities are slightly off-center longitudinally with respect to the coils (by 3.7 cm) to facilitate servicing; this will not affect beam-cooling performance. In addition, space for diagnostics is potentially available at that location, as detailed in Sec. 5.3.7.4. Note also that some rf feeds need to be tilted due to the space constraint imposed by the coupling coil cryostat. The piping and auxiliary hardware for the absorber shown in the figures correspond to the through-flow absorber design; they would, however, be very similar to those used in the convection absorber design.

Deviation from the simulation design driven by engineering or cost considerations will

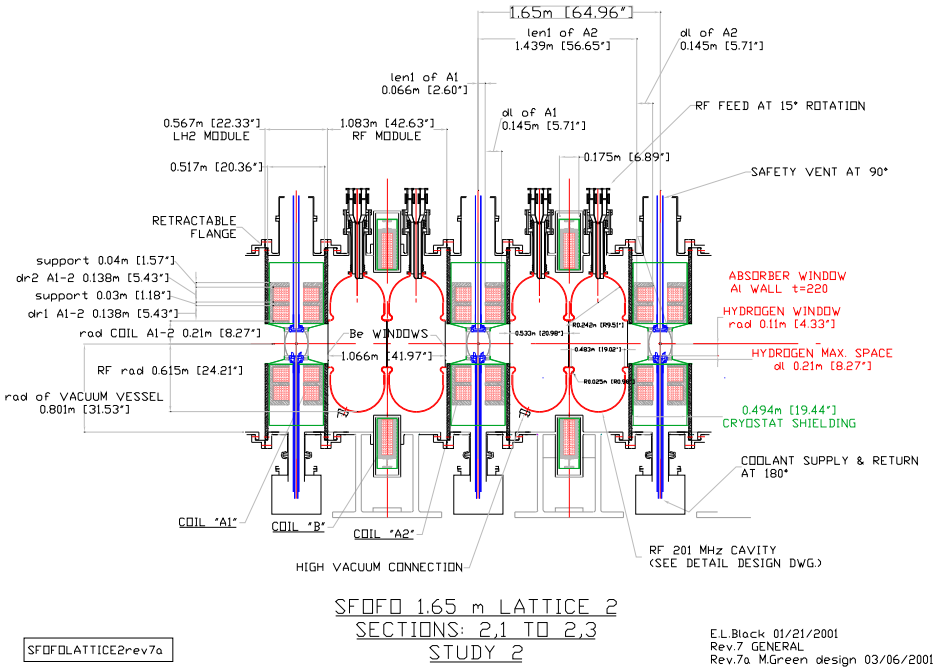

Figure 5.25: Engineering rendering of the 1.65 m cooling lattice cell.

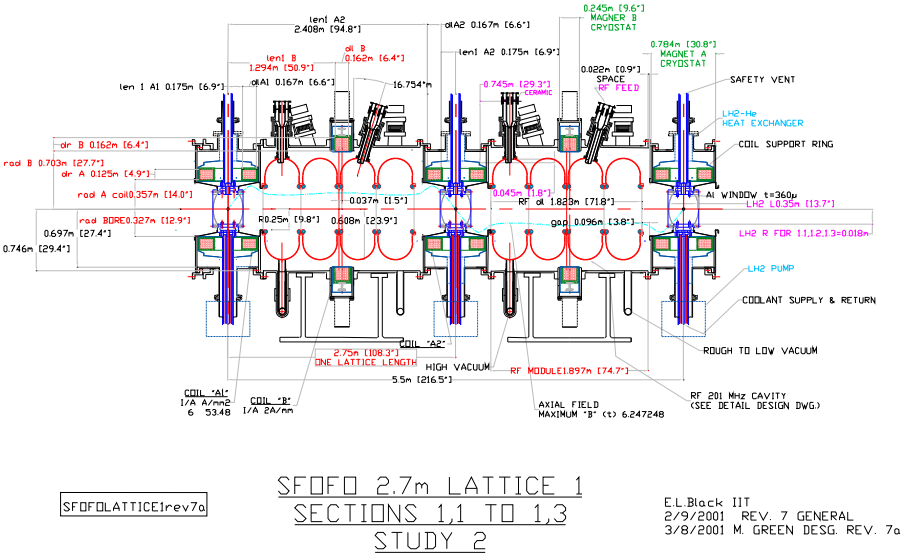

Figure 5.26: Engineering rendering of the 2.75 m cooling lattice cell.

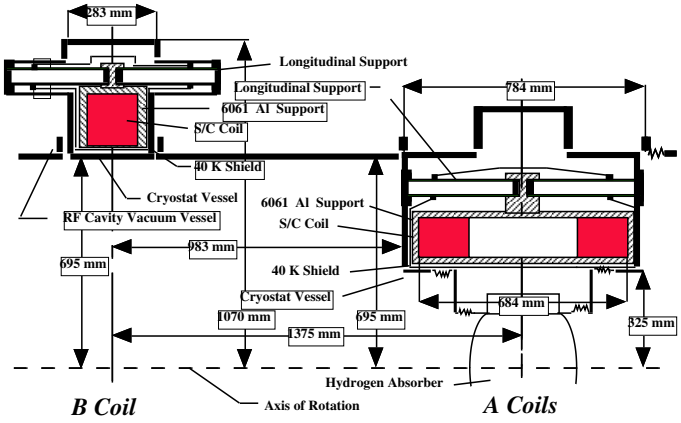

Figure 5.27: Magnet cross section for the 2.75 m long cooling cell. The coils labeled "A" is the focusing coil and "B" is the coupling coil.

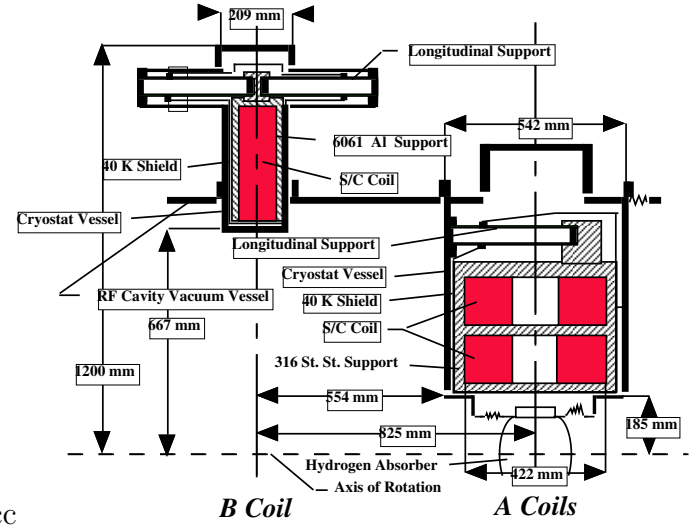

cc

Figure 5.28: Magnet cross section for the 1.65-m-long cooling cell. The coils labeled "A" is the focusing coil and "B" is the coupling coil.

most likely occur. Indeed, some items have been discovered in the course of this study and are listed below:

- Coil configuration: The coil positions, sizes, and current densities used in the simulations (see Tables 5.4–5.6) differ somewhat from those listed in Chapter 10, which have been engineered to reduce cost and to allow more room, both for the absorbers and for insertion of the rf feeds. We have verified that the revised fields on-axis are the same as for the original configuration, and that the slight discrepancies in the off-axis fields do not affect the cooling performance.

- Winding structural support: To handle the large forces exerted on the windings, the focusing coil ("A coil") in the (2,i) cooling lattices has been split into two windings with a structural stainless steel plate inserted in between (see Fig 5.28.) However, the simulations have been made assuming a current density uniformly distributed over the entire radius of the coil. We can easily readjust the current densities of these two windings to obtain the required magnetic field profile.

- Absorber details: Our simulation studies have assumed cylindrically-shaped liquid-hydrogen absorbers with flat windows of constant thickness. However, in practice the shape will be as indicated in Fig.5.22, with approximately spherical ends, and with tapered windows as shown in Fig. 5.21. A closer approximation has recently been implemented in Geant4, with the absorber ends represented as spherical caps and the correct window thickness profile, with no adverse effects on cooling performance.

- rf-window design: In the rf cavities used in the simulation, the beryllium windows are stepped in thickness, with their thickness suddenly increasing at the radius r_1 (see Chapter 8). In practice, the mass distribution near r_1 may well be smoother (for instance, if the change in thickness is brought about by means of chemical etching). We have verified that, as expected, a smooth transition does not affect the cooling performance.

5.4 Conclusion: Performance of the Entire Front End

The transverse emittance along the entire front end is plotted in Fig. 5.29. The emittance is seen to be reduced in the minicooling at 150 m (from 17 to 13 mm·rad), remains approximately constant through the induction linacs, althought large-amplitude particles are lost, and falls quickly in the final cooling section (from 12 to 2.8 mm·rad).

The muon-to-proton ratio along the full system is given in Fig. 5.30. Particle losses prior to the buncher come primarily from the loss of very high and very low momenta (30%), plus losses from muon decay ($\approx$ 20%). The losses in the cooling section come

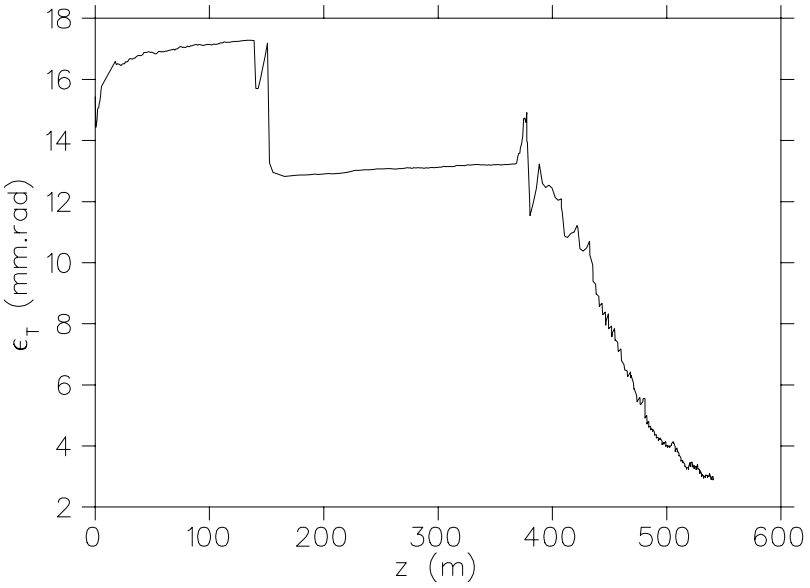

Figure 5.29: Transverse emittance as a function of distance along the front end.

from bunching inefficiency ($\approx 25\%$) and from loss of particles from the rf bucket as the longitudinal emittance grows in this section ($\approx 25\%$).

As shown in the left panel of Fig. 5.31, we are able to collect the muon phase space over a substancial kinetic energy range, *i.e.*, approximately 50–250 MeV. The peak collection efficiency occurs for kinetic energy around 100 MeV, where about 35% of the pions yield accepted muons. Note the falling efficiency for pions with kinetic energy above 300 MeV.

The SFOFO cooling channel increases the number of muons per proton in the 15 mm·rad transverse acceptance cut by a factor of 3.5, or a factor of 5.75 in the 9.35 mm·rad acceptance. This is the Geant4 estimate; ICOOL numbers, listed above, are slightly lower, consistent with systematic errors in the calculations. The factor of 5.75 should be compared with the corresponding enhancement achieved in Feasibility Study I, which was approximately 2 to 2.5 [3]. The better performance of the front-end is due primarily to our progress in understanding phase rotation and to the advantages of the SFOFO cooling lattice compared with the FOFO lattice used in Study-I.

Engineering and mechanical tolerances have been studied. We now know that such a channel can be assembled and aligned with known techniques.

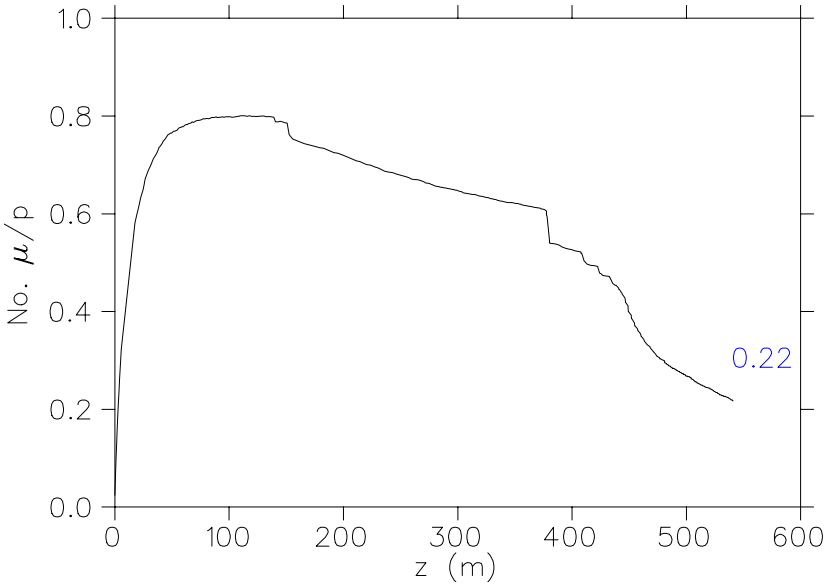

Figure 5.30: Muons per incident proton as a function of distance along the front end.

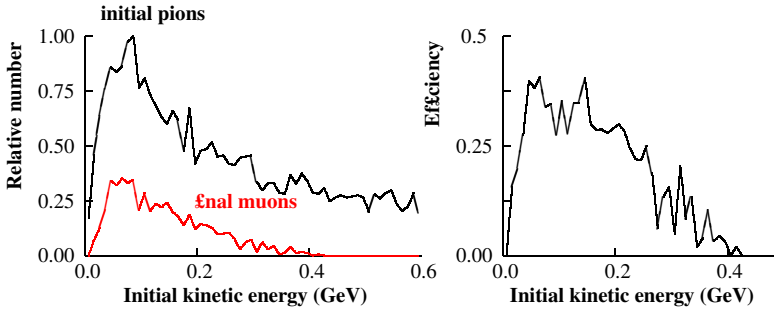

Figure 5.31: Left plot: Kinetic energy distribution of initial pions (upper curve) and of pions that decay into muons that exit the cooling channel (lower curve). Right plot: efficiency distribution for an initial pion to produce an accepted muon by the channel.

5.5 Matching Cooling to Acceleration

5.5.1 Method

The matching from the end of the cooling section to the start of the acceleration is achieved by adiabatically changing the lattice parameters from the short (1.65 m) low beta (0.18 m) SFOFO lattice (2,3) at the end of the cooling section to a longer (2.75 m) and higher beta (0.6 m) FOFO lattice. The transition is made in 10 cells.

Initially there are seven 1.65-m cells, all identical in dimensions, but with currents modified to gradually raise the central value of the beta function, and change the form of the beta function *vs.* momentum from the SFOFO shape (Fig. 5.5) to a monotonic slope. This is followed by 3 cells with all longitudinal dimensions scaled up to further increase the beta function. The beta functions at the ends of the various matching cells are shown as a function of momentum in Fig. 5.32.

Finally, after a lone coupling coil, followed by a reversed-direction coil to bring the axial field down to zero, the beta function is allowed to rise toward the value needed for the optics of the superconducting linac. Coil dimensions and axial fields are shown in Fig. 5.33.

5.5.2 RF Cavities

We introduce rf to keep the bunch together and to raise the average momentum. All currents are scaled with increasing momentum. The rf fields (on-crest) average 8 MV/m over 19 m. Average energy gain is 3 MV/m. Each cavity consists of two rf cells, except that there are three cells in cavity 10 and a single-cell cavity beyond the final focus coils, for a total of 22 cells. Each rf cell is identical to those in the 1.65-m cooling lattice. The total acceleration required (on crest) is 152 MeV, corresponding to 6.9 MeV per cell. The cavity phase is set to give an actual mean acceleration of 2.6 MeV per cavity.

5.5.3 Superconducting Coils

The coils have the same radial dimensions as those in the final cooling lattices, but different currents and, in the final cells, different lengths. Parameters of the matching coils are summarized in Table 5.9. The current densities in some coils are very low and the dimensions of the coils could be reduced, provided the total currents and current centers are maintained.

Table 5.9: Coil parameters for the cooling channel to acceleration section match.

Start (m)	dl (m)	r (m)	dr (m)	J (A/mm^2)
0.066	0.145	0.198	0.330	83.76
0.627	0.396	0.792	0.099	80.10
1.439	0.145	0.198	0.330	81.31
1.716	0.145	0.198	0.330	-81.66
2.277	0.396	0.792	0.099	-88.55
3.089	0.145	0.198	0.330	-78.99
3.366	0.145	0.198	0.330	79.32
3.927	0.396	0.792	0.099	95.67
4.739	0.145	0.198	0.330	77.58
5.016	0.145	0.198	0.330	-77.89
5.577	0.396	0.792	0.099	-103.02
6.389	0.145	0.198	0.330	-75.99
6.666	0.145	0.198	0.330	76.29
7.227	0.396	0.792	0.099	111.46
8.039	0.145	0.198	0.330	74.23
8.316	0.145	0.198	0.330	-74.52
8.877	0.396	0.792	0.099	-122.79
9.689	0.145	0.198	0.330	-72.31
9.966	0.145	0.198	0.330	72.58
10.527	0.396	0.792	0.099	130.03
11.339	0.145	0.198	0.330	73.92
11.616	0.145	0.198	0.330	-74.18
12.246	0.462	0.792	0.099	-106.28
13.193	0.169	0.198	0.330	-54.23
13.517	0.169	0.198	0.330	54.42
14.240	0.528	0.792	0.099	89.45
15.322	0.194	0.198	0.330	41.57
15.692	0.194	0.198	0.330	-41.71
16.509	0.594	0.792	0.099	-76.98
17.726	0.218	0.198	0.330	-32.94
18.142	0.218	0.198	0.330	29.74
19.052	0.660	0.792	0.099	47.20
21.378	0.660	0.792	0.099	-1.42

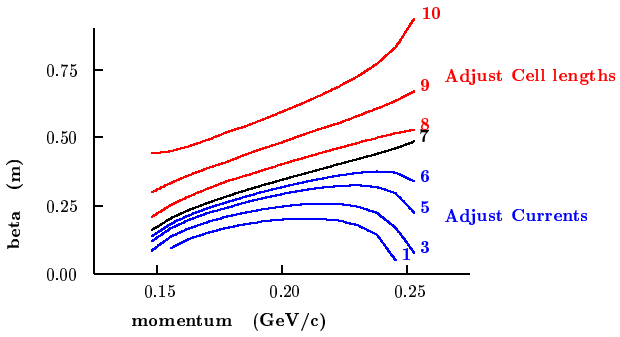

Figure 5.32: Beta functions at the end of various cells of the matching section.

5.5.4 ICOOL Simulation

Simulation of this matching section uses a file of tracks from the end of the baseline cooling simulation. It is important to point out that: i) No rf windows have yet been included in the simulations; ii) the window apertures have been set to 21 cm; and, iii) no optimization of the design has been attempted. We also note that the acceleration section was designed and without the present matching. Thus, the small amount of energy gain in the matching line will lead to the elimination of a portion ($\approx$ 39 m) of the initial preacceleration linac, described in Chapter 6. (This change was accounted for properly in the cost estimate)

Figures 5.34–5.37 show the behavior of a number of important quantities as a function of distance along the cooling-channel-to-acceleration-section matching line. The minimum of the β function shown in Fig. 5.34, varies from 18 cm at the beginning to $\approx$ 1 m at the end of the section. Figure 5.36 shows there is a net acceleration from 210 to 270 MeV/c, and also that the total muon loss due to the matching is only 1.25%. The loss inside the accelerator acceptance, shown in Fig. 5.37, is 2.4%. The selected μ/p ratios fluctuate because ECALC9 does not correct for angular momentum when it applies the transverse acceptance cuts. The values are correct only at locations where B_z is zero; these correspond to the maxima of μ/p in Fig. 5.37 (bottom). There is negligible growth in the normalized transverse and longitudinal emittances.

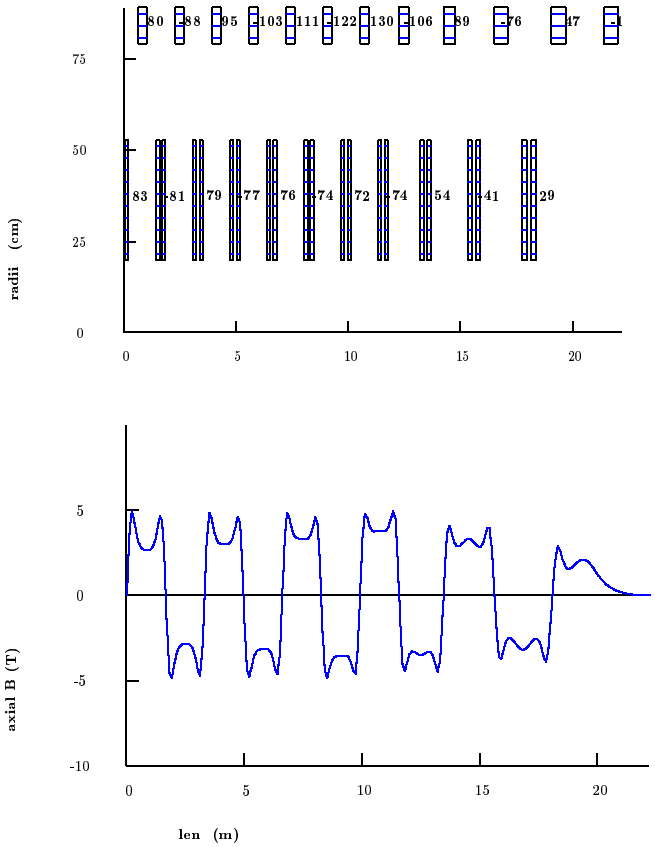

Figure 5.33: Coil dimensions and axial fields for the cooling-channel to acceleration-section matching section.

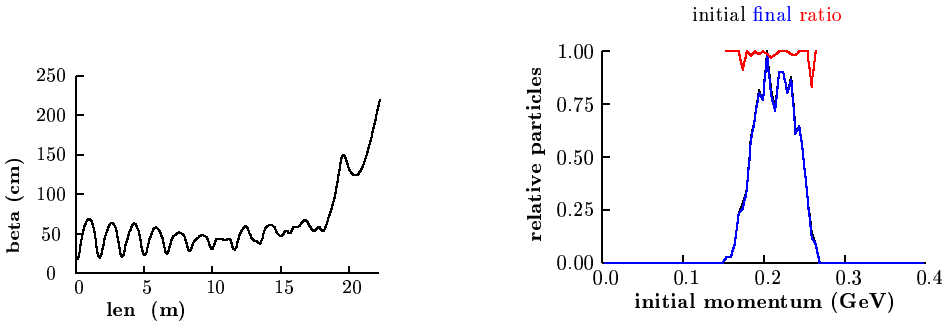

Figure 5.34: $\beta_\perp$ function *vs.* distance along the cooling-channel-to-acceleration-section matching (left); muon momentum distribution (right).

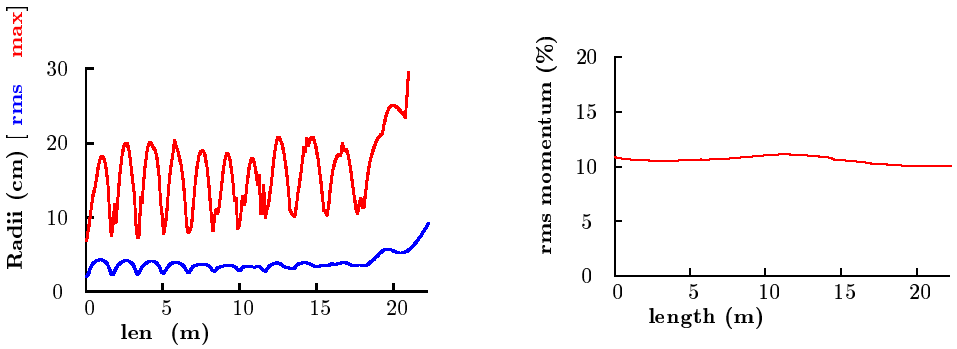

Figure 5.35: Rms and maximum radius *vs.* z (left); rms fractional momentum spread *vs.* z (right).

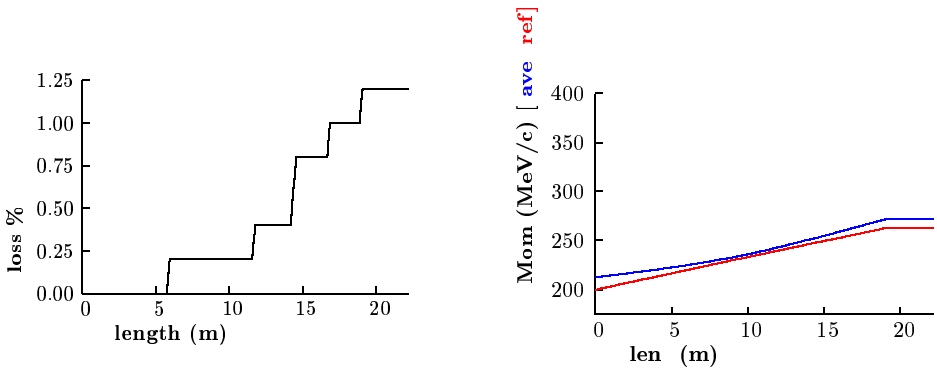

Figure 5.36: Loss in % (left); momentum *vs.* z (right), along the cooling-channel-to-acceleration-section matching line.

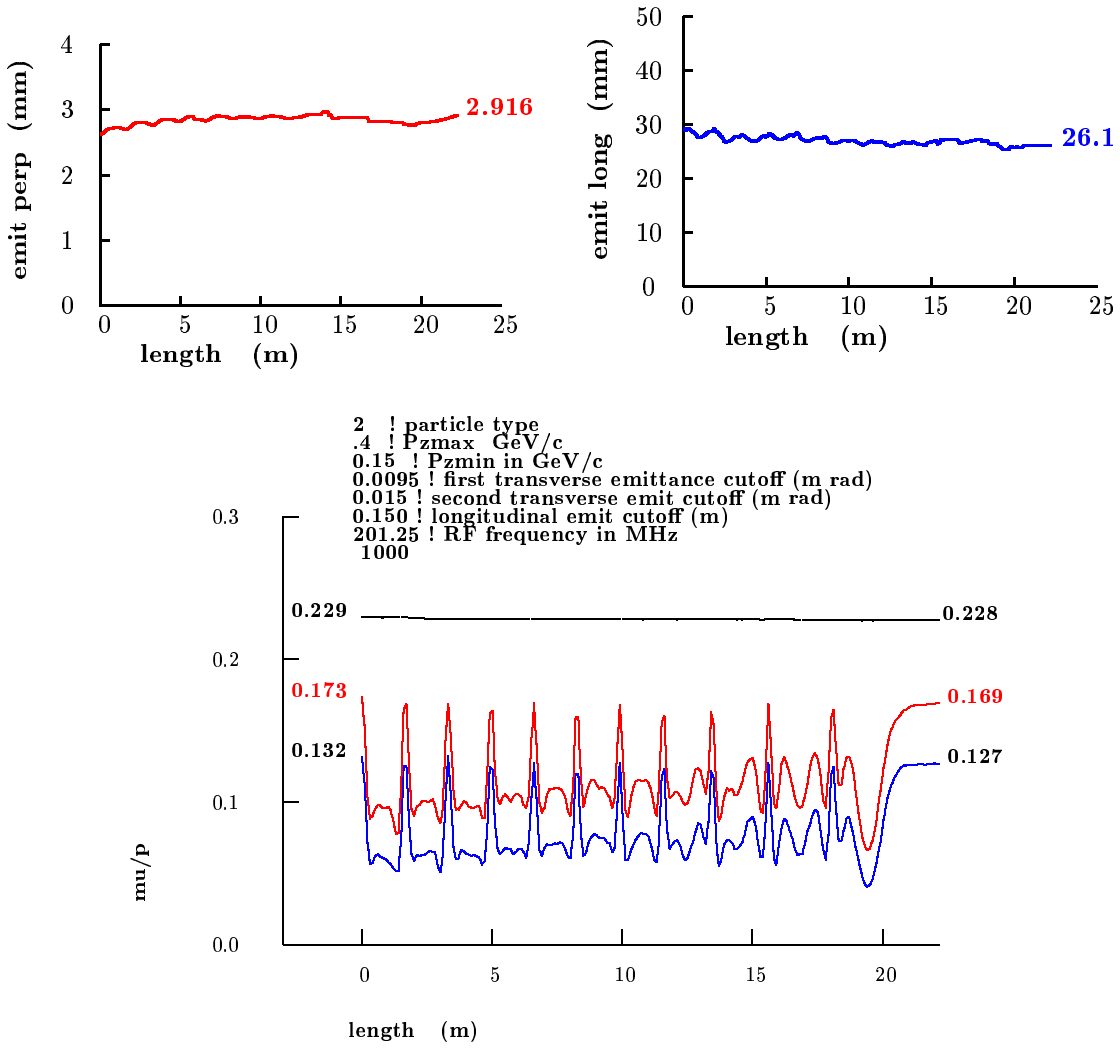

Figure 5.37: ϵ_T (top-left), ϵ_L (top-right), and μ/p (bottom) *vs.* z. The three curves in the bottom figure are: (top) total number of μ/p; (middle) within the ϵ_T=0.015 m·rad and ϵ_L=0.15 m cuts; (lower) within ϵ_T=0.0095 mm·rad and ϵ_L=0.15 m cuts.

Bibliography

[1] R. Fernow, *ICOOL, A Simulation Code for Ionization Cooling of Muons Beams*, Proceedings of the 1999 Particle Accelerator Conference, A. Lucio and W. MacKay, eds. (IEEE, Piscataway, NJ, 1999) p. 3020.

[2] The Geant4 Tool Kit is available at *http://wwwinfo.cern.ch/asd/geant4/geant4.html*

[3] *A Neutrino Source Based on an Intense Muon Storage Ring*, ed. N. Holtkamp and D. Finley, available at http://www.fnal.gov/projects/muon_collider/nu-factory/nu-factory.html

[4] C.M. Ankenbrandt *et al.* Phys. Rev. ST Accel. Beams 2, 081001 (1999)

[5] G. Penn *et al.*, Phys. Rev. Lett. 85 (4) pp. 764-767. July, (2000).

[6] J. Monroe *et al.*, *Design and Simulation of Muon Ionization Cooling Channels for the Fermilab Neutrino Factory Feasibility Study*, Phys. Rev. ST Accel. Beams 4, 041301 (2001).

[7] First suggested by A. Sessler, LBNL.

[8] The Particle Data Group, *Review of Particle Physics*, Eur. Phys. J. C **15** (2000) 163.

[9] This code was written by G. Penn, LBNL.

[10] R. Fernow, *Effect of a dipole error on the performance of the alternating solenoid lattice*, http://www-mucool.fnal.gov/mcnotes/muc0035.pdf

[11] P. Lebrun, *Sensitivity of the 15 T. Alternate Solenoid Cooling Channel to Dipole Errors caused by misalignment of the Solenoids*
http://www-mucool.fnal.gov/mcnotes/muc0073.ps

BIBLIOGRAPHY

[12] J. Gallardo, *Errors in a continuous solenoid* , http://www-mucool.fnal.gov/mcnotes/muc0041.ps; *Errors in a discrete solenoid* http://www-mucool.fnal.gov/mcnotes/muc0037.ps

[13] J. Gallardo, *Note on Vector potential for a Solenoid and Errors*, unpublished (1999).

[14] M. Bassetti and G.A. Erskine, *Closed Expression for the Electric Field of a Two-Dimensional Gaussian Charge*, CERN Report **CERN-ISR-TH/80-06**, 1980; S. Kheifets, *Potential of a Three-Dimensional Gaussian Bunch*, DESY Report **PETRA** Note 119 (1976).

[15] F. Zimmermann and T. Raubenheimer, *Longitudinal space charge in final-focus systems*, Nucl. Instrum. Meth., 1997; J. Gallardo, *Space Charge in Gaussian Beams: A Collection of formulas*, http://www-mucool.fnal.gov/mcnotes/muc0038.ps

[16] H. Wang, *Analytical approach to the short-range wakefields*, http://www-mucool.fnal.gov/mcnotes/muc0117.pdf

[17] MAFIA is available from CST GmbH, Buedinger Strasse 2a, 64289 Darmstadt, Germany (www.cst.de).

[18] J. Gallardo, *Implementing space-charge effects in cooling simulations*, BNL Report: Muon Tech. Notes Mu-019, 1998.

[19] J.W. Mark, SLAC-PUB-3169 (1984) and references therein.

[20] E.J. Beise *et al.*, Nucl. Instrum. Meth. **A378** (1996) 383.

[21] R.W. Carr *et al.*, SLAC-Proposal-E-158, July 1997.

[22] D.J. Margaziotis, in *Proc. CEBAF Summer 1992 Workshop*, F. Gross and R. Holt, eds., AIP Conf. Proc. **269**, American Institute of Physics, New York (1993), p. 531.

[23] R.W. Carr *et al.*, "E158 Liquid Hydrogen Target Milestone Report," April 21, 1999, http://www.slac.stanford.edu/exp/e158/documents/target.ps.gz.

[24] *ASME Boiler and Pressure Vessel Code*, ANSI/ASME BPV-VIII-1 (American Society of Mechanical Engineers, New York, 1980), part UG-32.

[25] J. Norem, *Instrumentation issues for the Neutrino Source* http://www-mucool.fnal.gov/mcnotes/muc0085.ps

[26] Kwang-Je Kim and Chun-xi Wang, Phys. Rev. Lett. **85** (760) 2000

[27] A. Blondel is working to develop a system based on a ring imaging Cerenkov technique.

[28] J. Norem, A. Moretti and M. Popovic, *The Radiation Environment in and near High Gradient RF Cavities*,
http://www-mucool.fnal.gov/mcnotes/muc0178.pdf

[29] M. Placidi *et al.*, *A CdTe Detector for Muon Transverse Profile Measurements*, CERN-NUFACT-Note 068, contributed to the MuCool Instrumentation Workshop, IIT, Chicago, Nov. 10-11 (2000).